# Strain gradient elasto-plasticity model: 3D isogeometric implementation and applications to cellular structures

Khakalo, Sergei; Laukkanen, Anssi

*Published in:*
Computer Methods in Applied Mechanics and Engineering

*DOI:*
10.1016/j.cma.2021.114225

Published: 01/01/2022

*Document Version*
Publisher's final version

Available online at www.sciencedirect.com
ScienceDirect
Comput. Methods Appl. Mech. Engrg. 388 (2022) 114225
Computer methods in applied mechanics and engineering
www.elsevier.com/locate/cma

# Strain gradient elasto-plasticity model: 3D isogeometric implementation and applications to cellular structures

Sergei Khakalo*, Anssi Laukkanen

*Integrated Computational Materials Engineering group, VTT Technical Research Centre of Finland, P.O. Box 1000, FI-02044 VTT, Finland*

Received 1 April 2021; received in revised form 14 September 2021; accepted 5 October 2021
Available online xxxx

**Abstract**

In the present work, we combine Mindlin's strain gradient elasticity theory and Gudmundson–Gurtin–Anand strain gradient plasticity theory to form a unified framework. The gradient plasticity model is enriched by including the gradient of elastic strains into the expression of the internal virtual work and free energy. This augments the modelling capabilities by incorporating elasticity-related length scales along with plasticity-related energetic and dissipative ones. The strong form governing equations are derived via the principle of virtual work addressing a complete set of boundary conditions. The fourth-order boundary value problem of the gradient elasto-plasticity model is then formulated in a variational form within an $H^2$ Sobolev space setting. Conforming Galerkin discretizations for numerical results are obtained utilizing an isogeometric approach with NURBS basis functions of degree $p \geq 2$ providing $C^{p-1}$-continuity. The implementation follows a viscoplastic constitutive framework and adopts the backward Euler time integration scheme. A set of benchmark examples is considered to illustrate convergence properties and to accomplish parameter studies. It is shown that the elastic length scale parameter controls the slope of the elastic part and causes an additional hardening in the plastic part of the material response curves. Finally, an illustrative example is considered in order to demonstrate the applicability of both the continuum model and the numerical method in capturing the size-dependent torsion response of cellular structures.


*Keywords:* Strain gradient elasticity; Strain gradient plasticity; Isogeometric analysis; Cellular structures; Size effects

## 1. Introduction

Development of strain gradient plasticity (SGP) theories, taking their origins in strain gradient and couple-stress elasticity theories [1–3], has been mainly motivated by experimental results reporting significant size-dependence of a yield strength and strain hardening especially for some metallic materials at micro scale [4–7]. While classical plasticity theories result in size-independent constitutive behaviour, in SGP theories internal length scales are incorporated through higher gradients of the kinematic and/or state variables reflecting microstructural effects at the continuum level. One of the first SGP formulations has been proposed in [8] (see also [9,10]), where the conventional yield function was modified by including the plastic strain gradient term. Further contributions have been developed

* Corresponding author.
*E-mail address:* sergei.khakalo@vtt.fi (S. Khakalo).

https://doi.org/10.1016/j.cma.2021.114225

by including the gradient of the local spin vector in [11], full second gradient of displacements in [12], or only the plastic strain gradient in [13] into the internal work (or power).

Works presented by Gudmundson [14] and Gurtin and Anand [15,16] for irrotational plastic flow and by Gurtin [17] for rotational plastic flow have formed a new class of SGP theories derived in a thermodynamically consistent framework. It has been proposed that, first, the higher-order microstresses are decomposed into energetic and dissipative parts and, second, the plastic flow direction, unlike in the previous SGP formulations, is governed by a microstress (in accordance with [18,19]) and not the deviatoric Cauchy stress. Along with a standard internal-variable hardening, the microstress decomposition brings two distinct physical phenomena, namely energetic hardening and dissipative (yield) strengthening [20]. Following the considerations in [14] and [21] that previously developed SGP models do not always fulfil the thermodynamic constraint, the corresponding reformulations have been provided in [22] and [23]. Besides aforementioned phenomenological SGP theories, there are developments of the so-called mechanism-based SGP theories [6,24–26], in which the density of geometrically necessary dislocations, enriching the shear flow stress, is directly related to the equivalent plastic strain gradient.

Microscale experimental observations of homogeneous metals reveal that the elasticity-related size effects are negligible with respect to the plasticity-related or even negligible at all [5,27,28]. This has pushed forward the development of SGP material models leaving the strain gradient elasto-plasticity (SGEP) models without proper attention. For the structures or mechanical metamaterials with highly noticeable, architected microstructure, the elasticity-related size effects become significant [29–35]. This has been utilized, for instance, for modelling and designing auxetic metamaterials with hierarchical structures leading to improved weight-to-stiffness characteristics [29,36]. Besides objects with marginal composition (with up to one unit cell in the thickness direction), classical continuum theories are shown to be insufficient for a proper modelling of objects with an infinite composition of unit cells when dealing with wave propagation phenomena [37–39]. Fast developing additive manufacturing technologies already made it possible to produce low-density lattice-based and cellular microstructures with an improved and even optimal isotropic stiffness [40,41], tolerant to damage [42], and mechanically robust [43], which paves the road for this class of (meta)materials towards engineering applications [44]. Direct (full-field) modelling of solids and structures with a lattice and cellular microarchitecture is, however, non-trivial and computationally costly. Alternatively, methods based on homogenization strategies and generalized continuum theories such as SGEP are considered to be a promising tool reflecting both the elasticity- and plasticity-related size effects.

Regarding numerical methods and analysis, non-classical plasticity theories require $C^1$-continuous solutions and/or involve additional degrees of freedom. Numerical issues of the Aifantis models [8,9] are discussed in [45,46] where $C^1$- and $C^0$-continuous finite element (FE) formulations are compared and analyzed. Numerical implementations of the Fleck–Hutchinson models [11,12] are presented in [47–49], where $C^1$-continuous elements and $C^0$-continuous (mixed) formulations are addressed. For the SGP version [13] of the Fleck–Hutchinson model [12], a straightforward numerical scheme involving $C^0$-continuous finite elements is proposed in [50].

For the Gudmundson–Gurtin–Anand theories with the irrotational plastic flow, rate-independent implementations are considered in [20,51,52]. A simplified 1D version of a model in [15] is numerically studied in [20] utilizing an Abaqus User Element (UEL) implementation with $C^0$ quadratic basis functions. A 2D plane strain UEL implementation of a model in [14] is accomplished in [51], which compares bilinear and biquadratic $C^0$-continuous finite elements and addresses numerical issues of the SGP model. The Fleck–Willis [53] SGP flow model is implemented in [52] within a 2D plane strain formulation with biquadratic interpolation for displacements and bilinear interpolation for plastic strains. Rate-dependent viscoplastic formulations are implemented in [54–57] within a 2D plane strain problem setting, which allowed to avoid challenges (inherent to the rate-independent flow formulations [52]) with the definition of yielding and further treatment of the evolution and interaction of plastic zones.

In the framework of theories with the rotational plastic flow [17], recently developed phenomenological SGP model, constitutively involving the plastic spin [58], has been proven to be a good isotropic approximation to describe the multislip behaviour predicted by a strain gradient crystal plasticity model [59,60]. The proposed model via 2D FE implementations has been utilized for solving various problems, such as torsion of thin circular wires [61], constrained simple shear and micro-bending of thin foils [62,63], crack growth resistance of metals [64], and fracture at bi-material interfaces [65].

A micromorphic approach [66] for SGP has been applied, for instance, in [67] for the phenomenological and in [68] for the crystal cases. Recent paper [69] offers Lagrange multiplier based and micromorphic gradient-enhanced crystal plasticity model, where the generalized modulus, related to the relative plastic strain, can be

interpreted as a numerical regularization parameter in order to implement SGP model [70]. Further details on strain gradient and higher-order (such as micropolar and micromorphic) continuum plasticity theories, numerical analyses and experimental investigations can be found in [71] and [72].

In the present work, we derive a phenomenological strain gradient elasto-plasticity continuum model following the irrotational plastic flow framework of Gudmundson, Gurtin and Anand SGP theories which are considered as constitutively local-type ones unlike [73], where arguments of nonlocal irreversible thermodynamics are employed. The present formulation is focused on the case of small strains and rotations. On one hand, the considered model can be categorized as a higher-order model (cf. [74]) since, as proposed in [14], it incorporates the higher-order microstress (or moment stress) as the work-conjugate to the plastic strain gradient. On the other hand, it can be also referred to as a higher-grade model due to an additional work-conjugate pair, namely the elastic strain gradient and the corresponding double stress, included in the present model. This results in fourth-order PDEs and brings additional BCs along with the non-conventional ones related to plastic strains. From the constitutive point of view, decomposition of the higher-order microstress into the energetic and dissipative parts brings the corresponding plasticity-related (dissipative and energetic) length scales, while the inclusion of the elastic strain gradients augments the model with additional elasticity-related length scales. This differs from the nonlocal-type SGEP model presented in [73], where only energetic contributions are considered.

The weak form of the boundary value problem for the present SGEP model is formulated within an $H^2$ Sobolev space setting incorporating first- and second-order spatial derivatives of the displacement and first-order spatial derivatives of the plastic strain variables requiring, in general, a $C^1$-continuity from the corresponding Galerkin methods. The conforming isogeometric Galerkin method is implemented using a 3D UEL within a commercial FE software Abaqus in a viscoplastic constitutive framework of [63,64]. The numerical realization is based on the backward Euler time integration scheme (cf. [50,55,74–76] based on the forward Euler integration schemes). With NURBS (Non-Uniform Rational B-Splines) shape functions of degree $p$ providing $C^{p-1}$-continuity Isogeometric Analysis (IGA), proposed in [77], naturally suits for solving the higher-order PDEs arising, e.g., in the Cahn–Hilliard phase-field models [78,79], Kirchhoff–Love shell model [80], gradient damage models [81], higher-order phase-field model for brittle fracture [82], and locking-free model for Reissner–Mindlin plates [83]. In the framework of (first and second) strain gradient elasticity theories, an IGA approach has been applied for 1D, 2D and 3D continuum models in [84–90], for models of structural beam elements in [91–94], plate elements in [95,96], and shells in [97]. Within SGP theories, isogeometric methods have been only recently utilized for analyses of second-order [98] and fourth-order [99] gradient-enhanced plasticity models (with adaptive hierarchical refinement of NURBS addressed in [100]).

The present paper is organized as follows. Section 2 is devoted to the derivation of the SGEP model with a strong formulation, addressing a full set of BCs, as well as with a weak formulation and its linearized form. Section 3 focuses on the formulation of the conforming isogeometric Galerkin method and addresses 3D implementation details. In Section 4, we consider a set of numerical benchmark examples, namely shear and bending of a strip, stretching of a plate weakened by a hole and torsion of a brick problems, and provide the convergence analysis and length scale parameter study. An application example is presented in Section 5, where both the elasticity- and plasticity-related size effects are captured by the SGEP model in a problem with torsion of structures possessing a cellular microarchitecture. Concluding remarks and some future steps are finally drawn in Section 6.

## 2. Strain gradient elasto-plasticity model

In the present paper, material nonlinearity is considered as the only nonlinearity source implying infinitesimal deformations. Therefore, additive decomposition of the total strain tensor $\boldsymbol{\varepsilon}$ into the elastic $\boldsymbol{\varepsilon}^e$ and plastic $\boldsymbol{\varepsilon}^p$ parts is assumed, which formally can be expressed as $\boldsymbol{\varepsilon} = \boldsymbol{\varepsilon}^e + \boldsymbol{\varepsilon}^p$.

### 2.1. Strong form

Starting from the SGP model presented in [14], where the elastic strains, plastic strains and plastic strain gradients contribute to the work per unit volume, the SGEP model is formulated by including in the internal virtual work $\delta W_{int}$ contributions from the elastic strain gradients, which can be expressed in the form

$$\delta W_{int} = \int_{\mathcal{B}} \left( \boldsymbol{\sigma} : \delta\boldsymbol{\varepsilon}^e + \boldsymbol{\tau} \vdots \delta\nabla\boldsymbol{\varepsilon}^e + \boldsymbol{q} : \delta\boldsymbol{\varepsilon}^p + \boldsymbol{m} \vdots \delta\nabla\boldsymbol{\varepsilon}^p \right) \mathrm{d}\mathcal{V} \tag{2.1}$$

or alternatively by expressing elastic strains in terms of total and plastic strains as

$$\delta W_{int} = \int_{\mathcal{B}} \left( \boldsymbol{\sigma} : \delta\boldsymbol{\varepsilon} + \boldsymbol{\tau} \vdots \delta\nabla\boldsymbol{\varepsilon} + \left(\boldsymbol{q} - \boldsymbol{\sigma}'\right) : \delta\boldsymbol{\varepsilon}^p + \left(\boldsymbol{m} - \boldsymbol{\tau}'\right) \vdots \delta\nabla\boldsymbol{\varepsilon}^p \right) \mathrm{d}\mathcal{V}, \tag{2.2}$$

where $\mathcal{B}$ is a volume occupied by a solid in a 3D space and $\nabla$ stands for the vector differential nabla-operator. The Cauchy stress and higher-order double stress tensors, the work conjugates to elastic strain and elastic strain gradient tensors, are denoted, respectively, by $\boldsymbol{\sigma}$ and $\boldsymbol{\tau}$. The corresponding deviatoric parts are represented by $\boldsymbol{\sigma}'$ and $\boldsymbol{\tau}'$. The work conjugates to plastic strain and plastic strain gradient tensors are defined, respectively, as (in [14]) microstresses $\boldsymbol{q}$ and (higher-order) moment stresses $\boldsymbol{m}$. Since the plastic volume changes are neglected, making the plastic strain tensor equal to its deviatoric part, only the deviatoric parts of the microstresses and moment stresses contribute to the internal virtual work. Hence, here and in what follows, $\boldsymbol{q}$ and $\boldsymbol{m}$ will stand for the deviatoric parts of the microstress and moment stress tensors.

Applying the divergence theorem and Stoke's theorem (see [2,101–103] for derivation details within strain gradient elasticity theory) and representing the total strains in terms of displacements $\boldsymbol{u}$ as $\boldsymbol{\varepsilon} = (\nabla\boldsymbol{u} + \boldsymbol{u}\nabla)/2$, internal virtual work (2.2) for independent variations $\delta\boldsymbol{u}$ and $\delta\boldsymbol{\varepsilon}^p$ expands as

$$\begin{aligned}
\delta W_{int} = &- \int_{\mathcal{B}} \nabla\cdot(\boldsymbol{\sigma} - \nabla\cdot\boldsymbol{\tau})\cdot\delta\boldsymbol{u}\mathrm{d}\mathcal{V} - \int_{\mathcal{B}} \left(\nabla\cdot\left(\boldsymbol{m} - \boldsymbol{\tau}'\right) + \boldsymbol{\sigma}' - \boldsymbol{q}\right) : \delta\boldsymbol{\varepsilon}^p \mathrm{d}\mathcal{V} \\
&+ \int_{\partial\mathcal{B}} (\boldsymbol{n}\cdot(\boldsymbol{\sigma} - \nabla\cdot\boldsymbol{\tau}) + [\boldsymbol{n}(\nabla_s\cdot\boldsymbol{n}) - \nabla_s]\cdot(\boldsymbol{n}\cdot\boldsymbol{\tau}))\cdot\delta\boldsymbol{u}\mathrm{d}\mathcal{S} \\
&+ \int_{\partial\mathcal{B}} \boldsymbol{n}\boldsymbol{n} : \boldsymbol{\tau}\cdot\frac{\partial}{\partial n}\delta\boldsymbol{u}\mathrm{d}\mathcal{S} + \int_{\partial\mathcal{B}} \boldsymbol{n}\cdot\left(\boldsymbol{m} - \boldsymbol{\tau}'\right) : \delta\boldsymbol{\varepsilon}^p\mathrm{d}\mathcal{S} \\
&+ \int_{\Gamma(\mathcal{B})} [\![\boldsymbol{n}\boldsymbol{l} : \boldsymbol{\tau}]\!]\cdot\delta\boldsymbol{u}\mathrm{d}\mathcal{C},
\end{aligned} \tag{2.3}$$

which introduces the following traction vectors and tensors expressed in terms of stress quantities:

$$\boldsymbol{T} = \boldsymbol{n}\cdot(\boldsymbol{\sigma} - \nabla\cdot\boldsymbol{\tau}) + [\boldsymbol{n}(\nabla_s\cdot\boldsymbol{n}) - \nabla_s]\cdot(\boldsymbol{n}\cdot\boldsymbol{\tau}), \tag{2.4}$$

$$\boldsymbol{R} = \boldsymbol{n}\boldsymbol{n} : \boldsymbol{\tau}, \tag{2.5}$$

$$\boldsymbol{Q} = [\![\boldsymbol{n}\boldsymbol{l} : \boldsymbol{\tau}]\!], \tag{2.6}$$

$$\boldsymbol{M} = \boldsymbol{n}\cdot\left(\boldsymbol{m} - \boldsymbol{\tau}'\right). \tag{2.7}$$

Here, $\boldsymbol{T}$ is the surface force per unit area (or traction force), $\boldsymbol{R}$ denotes a double force per unit area (or double traction force), $\boldsymbol{Q}$ stands for a line force per unit length (or line traction force), and $\boldsymbol{M}$ is to be interpreted as a (plastic) surface moment per unit area (or traction moment). The bold face brackets $[\![(\cdot)]\!]$ denote the jump of the enclosed quantity which is discontinuous across $\Gamma(\mathcal{B})$, where edge line $\Gamma(\mathcal{B})$ is formed by two mutually intersecting surfaces. For $\boldsymbol{s}$, denoting a unit vector tangential to $\Gamma(\mathcal{B})$, and $\boldsymbol{n}$, standing for an outward normal to $\partial\mathcal{B}$ unit vector, $\boldsymbol{l}$ is introduced as $\boldsymbol{l} = \boldsymbol{s}\times\boldsymbol{n}$. The decomposition $\nabla = \boldsymbol{n}\partial_n + \nabla_s$ defines a surface (or tangential) nabla-operator $\nabla_s$ with $\partial_n$ being a notation for partial derivative $\partial/\partial_n$.

Form of expression (2.3) suggests the following construction of the variation of work done by external forces

$$\begin{aligned}
\delta W_{ext} = &\int_{\mathcal{B}} \boldsymbol{f}\cdot\delta\boldsymbol{u}\mathrm{d}\mathcal{V} + \int_{\mathcal{B}} \boldsymbol{r} : \delta\boldsymbol{\varepsilon}^p\mathrm{d}\mathcal{V} \\
&+ \int_{\partial\mathcal{B}} \boldsymbol{F}_T\cdot\delta\boldsymbol{u}\mathrm{d}\mathcal{S} + \int_{\partial\mathcal{B}} \boldsymbol{F}_R\cdot\frac{\partial}{\partial n}\delta\boldsymbol{u}\mathrm{d}\mathcal{S} + \int_{\partial\mathcal{B}} \boldsymbol{F}_M : \delta\boldsymbol{\varepsilon}^p\mathrm{d}\mathcal{S} \\
&+ \int_{\Gamma(\mathcal{B})} \boldsymbol{F}_Q\cdot\delta\boldsymbol{u}\mathrm{d}\mathcal{C},
\end{aligned} \tag{2.8}$$

where $\boldsymbol{f}$ stands for the body force vector per unit volume, $\boldsymbol{r}$ is to be interpreted as a (plastic) body moment tensor per unit volume, $\boldsymbol{F}_T$, $\boldsymbol{F}_R$, $\boldsymbol{F}_Q$, and $\boldsymbol{F}_M$ are, respectively, external traction force, external double traction force, external line traction force, and external traction moment. It should be noted that without terms containing variations of the plastic strains, form (2.8) is similar to the one proposed in [2] within strain gradient elasticity theory.

Following the principle of virtual work (PVW) formally expressed as $\delta W_{int} = \delta W_{ext}$, for arbitrary $\delta\boldsymbol{u}$ and $\delta\boldsymbol{\varepsilon}^p$, the governing differential equation is obtained in terms of stresses in the form

$$\nabla\cdot(\boldsymbol{\sigma} - \nabla\cdot\boldsymbol{\tau}) + \boldsymbol{f} = 0,$$

$$\nabla \cdot \left(\boldsymbol{m} - \boldsymbol{\tau}'\right) + \boldsymbol{\sigma}' - \boldsymbol{q} + \boldsymbol{r} = 0 \quad \text{in } \mathcal{B}. \tag{2.9}$$

A set of boundary conditions is defined as follows

$$\begin{aligned} \boldsymbol{u} &= \boldsymbol{u}_T \quad \text{or} \quad \boldsymbol{T} = \boldsymbol{F}_T \quad \text{on } \partial\mathcal{B}, \\ \frac{\partial}{\partial n}\boldsymbol{u} &= \boldsymbol{u}_R \quad \text{or} \quad \boldsymbol{R} = \boldsymbol{F}_R \quad \text{on } \partial\mathcal{B}, \\ \boldsymbol{u} &= \boldsymbol{u}_Q \quad \text{or} \quad \boldsymbol{Q} = \boldsymbol{F}_Q \quad \text{on } \Gamma(\mathcal{B}), \\ \boldsymbol{\varepsilon}^p &= \boldsymbol{\varepsilon}_M \quad \text{or} \quad \boldsymbol{M} = \boldsymbol{F}_M \quad \text{on } \partial\mathcal{B}, \end{aligned} \tag{2.10}$$

where either the primary variables are prescribed (via given values $\boldsymbol{u}_T$, $\boldsymbol{u}_R$, $\boldsymbol{u}_Q$, and $\boldsymbol{\varepsilon}_M$) or the corresponding dual variables, i.e., traction vectors and tensors, are specified.

### 2.2. Constitutive laws

By analogy with the internal virtual work, a free energy per unit volume $\psi$ is constructed to depend in the general case on $\boldsymbol{\varepsilon}^e$, $\nabla\boldsymbol{\varepsilon}^e$, $\boldsymbol{\varepsilon}^p$ and $\nabla\boldsymbol{\varepsilon}^p$. For centrosymmetric materials, $\psi$ can be written in the following form (also considered in [73])

$$\psi = \frac{1}{2}\boldsymbol{\varepsilon}^e : \boldsymbol{C} : \boldsymbol{\varepsilon}^e + \frac{1}{2}\nabla\boldsymbol{\varepsilon}^e \vdots \boldsymbol{A} \vdots \nabla\boldsymbol{\varepsilon}^e + \psi_{\nabla\varepsilon^p}(\nabla\boldsymbol{\varepsilon}^p) + \psi_{\varepsilon^p}(\boldsymbol{\varepsilon}^p), \tag{2.11}$$

where $\boldsymbol{C}$ stands for the tensor of classical elastic moduli and $\boldsymbol{A}$ stands for the tensor of higher-order elastic moduli.

**Remark 1.** Since plastic deformation process is assumed to be dissipative in general, the $\psi_{\varepsilon^p}(\boldsymbol{\varepsilon}^p)$-contribution will be excluded. However, in [104], it is pointed out that according to the dislocation mechanisms the materials might exhibit two kinds (energetic and dissipative) of thermodynamic activities.

Following the second law of thermodynamics formulated in the form of Clausius–Duhem inequality, the dissipation inequality takes the following form (cf. [14], where within the SGP model gradients of the elastic strains are not considered)

$$\begin{aligned} \int_{\mathcal{B}} \Bigg[ &\left(\boldsymbol{\sigma} - \frac{\partial\psi}{\partial\boldsymbol{\varepsilon}^e}\right) : \dot{\boldsymbol{\varepsilon}}^e + \left(\boldsymbol{\tau} - \frac{\partial\psi}{\partial\nabla\boldsymbol{\varepsilon}^e}\right) \vdots \nabla\dot{\boldsymbol{\varepsilon}}^e \\ &+ \left(\boldsymbol{q} - \frac{\partial\psi}{\partial\boldsymbol{\varepsilon}^p}\right) : \dot{\boldsymbol{\varepsilon}}^p + \left(\boldsymbol{m} - \frac{\partial\psi}{\partial\nabla\boldsymbol{\varepsilon}^p}\right) \vdots \nabla\dot{\boldsymbol{\varepsilon}}^p \Bigg] \, \mathrm{d}\mathcal{V} \geq 0, \end{aligned} \tag{2.12}$$

where the dissipation rate is formed as the difference between the internal work rate and the rate of change in free energy. The classical constitutive relation in the form of generalized Hooke's law and the corresponding higher-order analogue can be immediately retrieved as

$$\boldsymbol{\sigma} = \frac{\partial\psi}{\partial\boldsymbol{\varepsilon}^e} = \boldsymbol{C} : \boldsymbol{\varepsilon}^e, \quad \boldsymbol{\tau} = \frac{\partial\psi}{\partial\nabla\boldsymbol{\varepsilon}^e} = \boldsymbol{A} \vdots \nabla\boldsymbol{\varepsilon}^e. \tag{2.13}$$

For isotropic materials, these expressions are rewritten in terms of the Lamé constants $\mu$ and $\lambda$ in the form

$$\boldsymbol{\sigma} = 2\mu\boldsymbol{\varepsilon}^e + \lambda\mathrm{tr}(\boldsymbol{\varepsilon}^e)\boldsymbol{I}, \quad \boldsymbol{\tau} = L_g^2\left(2\mu\nabla\boldsymbol{\varepsilon}^e + \lambda\nabla\mathrm{tr}(\boldsymbol{\varepsilon}^e)\boldsymbol{I}\right), \tag{2.14}$$

where regarding the strain gradient-elastic part a weakly non-local isotropy (see [105]) is considered, which coincides with the so-called simplified strain gradient model [106] introducing only one elastic length scale parameter $L_g$ with unit of length.

**Remark 2.** In a general case of centrosymmetry and isotropy, the gradient-elastic material model brings five additional higher-order constitutive constants [2]. The one-parameter gradient-elastic model is utilized in the current work for sake of simplicity of the numerical implementation which can be extended to the full five-parameter model (as well as to any intermediate model [107]) in a natural way.

Since the dissipative inequality is valid for every volume element, an integral representation (2.12) can be expressed in the following local form [14]

$$\boldsymbol{q}^D : \dot{\boldsymbol{\varepsilon}}^p + \boldsymbol{m}^D \vdots \nabla\dot{\boldsymbol{\varepsilon}}^p \geq 0, \tag{2.15}$$

where the quantities in front of the plastic strain rate and plastic strain gradient rate are the dissipative (or unrecoverable) parts of, respectively, the microstresses and moment stresses [14]

$$\boldsymbol{q}^D = \boldsymbol{q} - \frac{\partial\psi}{\partial\boldsymbol{\varepsilon}^p}, \quad \boldsymbol{m}^D = \boldsymbol{m} - \frac{\partial\psi}{\partial\nabla\boldsymbol{\varepsilon}^p}. \tag{2.16}$$

The partial derivatives of the free energy with respect to the plastic strains and plastic strain gradients define the energetic parts of the corresponding stresses. Since we assume that plastic strains do not contribute to the free energy, the energetic microstresses vanish, i.e., $\boldsymbol{q}^D = \boldsymbol{q}$. Regarding the energetic moment stresses the corresponding part of the free energy is taken in the following form

$$\psi_{\nabla\varepsilon^p}(\nabla\boldsymbol{\varepsilon}^p) = \mu L_e^2 \nabla\boldsymbol{\varepsilon}^p \vdots \nabla\boldsymbol{\varepsilon}^p, \tag{2.17}$$

which leads to the following representation of the energetic moment stresses

$$\boldsymbol{m}^E = \frac{\partial\psi}{\partial\nabla\boldsymbol{\varepsilon}^p} = 2\mu L_e^2 \nabla\boldsymbol{\varepsilon}^p, \tag{2.18}$$

where $L_e$ stands for the energetic length scale parameter with unit of length.

**Remark 3.** In the present work a quadratic free (or defect) energy in plastic strain gradients is adopted (see [108] for a general power-law defect energy computational study). As an alternative candidate, motivated by the work [109], a logarithmic defect energy with respect to the dislocation density tensor (related to a curl of the plastic distortion tensor) is considered in [68,110] and is shown to provide a continuum formulation of Asaro's type III kinematic hardening model.

An effective equivalent stress is defined as a quadratic form in the dissipative stresses as [14]

$$\Sigma = \sqrt{\frac{3}{2}\boldsymbol{q}^D : \boldsymbol{q}^D + \frac{1}{L_p^2}\boldsymbol{m}^D \vdots \boldsymbol{m}^D}, \tag{2.19}$$

whereas an effective equivalent plastic strain rate is introduced in the form [14]

$$\dot{E}^p = \sqrt{\frac{2}{3}\dot{\boldsymbol{\varepsilon}}^p : \dot{\boldsymbol{\varepsilon}}^p + L_p^2 \nabla\dot{\boldsymbol{\varepsilon}}^p \vdots \nabla\dot{\boldsymbol{\varepsilon}}^p}, \tag{2.20}$$

where $L_p$ denotes the dissipative length scale parameter with unit of length. The dissipative stress quantities are prescribed in terms of rates of the plastic strains and plastic strain gradients in the form [17,55]

$$\boldsymbol{q}^D = \frac{2}{3}\frac{\Sigma}{\dot{E}^p}\dot{\boldsymbol{\varepsilon}}^p, \quad \boldsymbol{m}^D = L_p^2 \frac{\Sigma}{\dot{E}^p}\nabla\dot{\boldsymbol{\varepsilon}}^p, \tag{2.21}$$

which makes $\Sigma$ and $\dot{E}^p$ work conjugate quantities and allows to rewrite dissipative inequality (2.15) as $\Sigma\dot{E}^p \geq 0$.

**Remark 4.** It should be noted that an orthogonal decomposition of third-order tensors $\nabla\boldsymbol{\varepsilon}^p$ and $\boldsymbol{m}$ allows to introduce three energetic and three dissipative length scale parameters with units of length [13]. However, for simplicity, only one energetic $L_e$ and one dissipative $L_p$ length scale parameters are considered in our work.

### 2.3. Weak formulations

For solving problems within the nonlinear SGEP model, an incremental solution procedure [111] is employed. Given the solution at time $n$, we seek the displacement and plastic strain increments $\Delta\boldsymbol{u}$ and $\Delta\boldsymbol{\varepsilon}^p$, respectively, to obtain the solution at time $n+1$

$$^{n+1}\boldsymbol{u} = {}^{n}\boldsymbol{u} + \Delta\boldsymbol{u}, \quad {}^{n+1}\boldsymbol{\varepsilon}^p = {}^{n}\boldsymbol{\varepsilon}^p + \Delta\boldsymbol{\varepsilon}^p. \tag{2.22}$$

The stresses, evaluated from the total displacements and plastic strains, satisfy the PVW at time $n+1$, which is given in the variational (or weak) form as follows:

For ${}^{n+1}\boldsymbol{f} \in [L^2(\mathcal{B})]^3$ and ${}^{n+1}\boldsymbol{r} \in [L^2(\mathcal{B})]^6$, find $({}^{n+1}\boldsymbol{u}, {}^{n+1}\boldsymbol{\varepsilon}^p) \in \boldsymbol{\mathcal{U}} \times \boldsymbol{\mathcal{E}}$ such that

$$a({}^{n+1}\boldsymbol{u}, {}^{n+1}\boldsymbol{\varepsilon}^p; \bar{\boldsymbol{u}}, \bar{\boldsymbol{\varepsilon}}) = l(\bar{\boldsymbol{u}}, \bar{\boldsymbol{\varepsilon}}), \quad \forall (\bar{\boldsymbol{u}}, \bar{\boldsymbol{\varepsilon}}) \in \bar{\boldsymbol{\mathcal{U}}} \times \bar{\boldsymbol{\mathcal{E}}}, \tag{2.23}$$

where the bilinear form $a$: $(\boldsymbol{\mathcal{U}} \times \boldsymbol{\mathcal{E}}) \times (\bar{\boldsymbol{\mathcal{U}}} \times \bar{\boldsymbol{\mathcal{E}}}) \to \mathbb{R}$ and load functional $l$: $\bar{\boldsymbol{\mathcal{U}}} \times \bar{\boldsymbol{\mathcal{E}}} \to \mathbb{R}$ are defined as

$$\begin{aligned} a({}^{n+1}\boldsymbol{u}, {}^{n+1}\boldsymbol{\varepsilon}^p; \bar{\boldsymbol{u}}, \bar{\boldsymbol{\varepsilon}}) = \int_{\mathcal{B}} \big( & {}^{n+1}\boldsymbol{\sigma} : \boldsymbol{\varepsilon}(\bar{\boldsymbol{u}}) + {}^{n+1}\boldsymbol{\tau} \vdots \nabla \boldsymbol{\varepsilon}(\bar{\boldsymbol{u}}) \\ & + {}^{n+1}\big(\boldsymbol{q}^D - \boldsymbol{\sigma}'\big) : \bar{\boldsymbol{\varepsilon}} + {}^{n+1}\big(\boldsymbol{m} - \boldsymbol{\tau}'\big) \vdots \nabla \bar{\boldsymbol{\varepsilon}} \big) \mathrm{d}\mathcal{V}, \end{aligned} \tag{2.24}$$

$$l(\bar{\boldsymbol{u}}, \bar{\boldsymbol{\varepsilon}}) = \int_{\mathcal{B}} \big( {}^{n+1}\boldsymbol{f} \cdot \bar{\boldsymbol{u}} + {}^{n+1}\boldsymbol{r} : \bar{\boldsymbol{\varepsilon}} \big) \mathrm{d}\mathcal{V}, \tag{2.25}$$

where for brevity only body forces are included in the load functional. The trial function spaces are defined as

$$\boldsymbol{\mathcal{U}} = \{\boldsymbol{u} \in [H^2(\mathcal{B})]^3 \mid \boldsymbol{u}_{|\partial\mathcal{B}_1} = \boldsymbol{u}_1, \ \frac{\partial \boldsymbol{u}}{\partial n}|_{\partial\mathcal{B}_2} = \boldsymbol{u}_2\}, \tag{2.26}$$

$$\boldsymbol{\mathcal{E}} = \{\boldsymbol{\eta} \in [H^1(\mathcal{B})]^6 \mid \boldsymbol{\eta}_{|\partial\mathcal{B}_3} = \boldsymbol{\varepsilon}_1\}, \tag{2.27}$$

with given Dirichlet data $\boldsymbol{u}_1$, $\boldsymbol{u}_2$, $\boldsymbol{\varepsilon}_1$ and with $\partial\mathcal{B}_D = \partial\mathcal{B}_1 \cup \partial\mathcal{B}_2 \cup \partial\mathcal{B}_3$ denoting the Dirichlet part of the boundary, whereas test function spaces $\bar{\boldsymbol{\mathcal{U}}}$ and $\bar{\boldsymbol{\mathcal{E}}}$ consist, respectively, of $H^2$ and $H^1$ functions satisfying the corresponding homogeneous Dirichlet boundary conditions.

The solution to the nonlinear problem defined in (2.23) is achieved utilizing the Newton–Raphson iterative method. The linearized form of the corresponding variational formulation reads as follows:

For ${}^{n+1}\boldsymbol{f} \in [L^2(\mathcal{B})]^3$ and ${}^{n+1}\boldsymbol{r} \in [L^2(\mathcal{B})]^6$, find $(\Delta\boldsymbol{u}_{(k)}, \Delta\boldsymbol{\varepsilon}^p_{(k)}) \in \boldsymbol{\mathcal{U}} \times \boldsymbol{\mathcal{E}}$ such that

$$a^*(\Delta\boldsymbol{u}_{(k)}, \Delta\boldsymbol{\varepsilon}^p_{(k)}; \bar{\boldsymbol{u}}, \bar{\boldsymbol{\varepsilon}}) = l(\bar{\boldsymbol{u}}, \bar{\boldsymbol{\varepsilon}}) - a({}^{n+1}\boldsymbol{u}_{(k)}, {}^{n+1}\boldsymbol{\varepsilon}^p_{(k)}; \bar{\boldsymbol{u}}, \bar{\boldsymbol{\varepsilon}}), \tag{2.28}$$

$\forall (\bar{\boldsymbol{u}}, \bar{\boldsymbol{\varepsilon}}) \in \bar{\boldsymbol{\mathcal{U}}} \times \bar{\boldsymbol{\mathcal{E}}}$, where the bilinear form $a$: $(\boldsymbol{\mathcal{U}} \times \boldsymbol{\mathcal{E}}) \times (\bar{\boldsymbol{\mathcal{U}}} \times \bar{\boldsymbol{\mathcal{E}}}) \to \mathbb{R}$ and load functional $l$: $\bar{\boldsymbol{\mathcal{U}}} \times \bar{\boldsymbol{\mathcal{E}}} \to \mathbb{R}$ are defined in (2.24) and (2.25), respectively. Here, the bilinear form $a^*$: $(\boldsymbol{\mathcal{U}} \times \boldsymbol{\mathcal{E}}) \times (\bar{\boldsymbol{\mathcal{U}}} \times \bar{\boldsymbol{\mathcal{E}}}) \to \mathbb{R}$ denotes the directional derivative (cf. [112]) of bilinear form (2.24) at a solution estimate $({}^{n+1}\boldsymbol{u}_{(k)}, {}^{n+1}\boldsymbol{\varepsilon}^p_{(k)})$ in the direction of increments $(\Delta\boldsymbol{u}_{(k)}, \Delta\boldsymbol{\varepsilon}^p_{(k)})$ and is defined as

$$\begin{aligned} & a^*(\Delta\boldsymbol{u}_{(k)}, \Delta\boldsymbol{\varepsilon}^p_{(k)}; \bar{\boldsymbol{u}}, \bar{\boldsymbol{\varepsilon}}) = Da({}^{n+1}\boldsymbol{u}_{(k)}, {}^{n+1}\boldsymbol{\varepsilon}^p_{(k)}; \bar{\boldsymbol{u}}, \bar{\boldsymbol{\varepsilon}})[\Delta\boldsymbol{u}_{(k)}, \Delta\boldsymbol{\varepsilon}^p_{(k)}] \\ & = \int_{\mathcal{B}} \Bigg( \boldsymbol{\varepsilon}(\bar{\boldsymbol{u}}) : \Big( \boldsymbol{C} : \boldsymbol{\varepsilon}(\Delta\boldsymbol{u}_{(k)}) - \boldsymbol{C}' : \Delta\boldsymbol{\varepsilon}^p_{(k)} \Big) \\ & + \nabla\boldsymbol{\varepsilon}(\bar{\boldsymbol{u}}) \vdots \Big( \boldsymbol{A} \vdots \nabla\boldsymbol{\varepsilon}(\Delta\boldsymbol{u}_{(k)}) - \boldsymbol{A}' \vdots \nabla\Delta\boldsymbol{\varepsilon}^p_{(k)} \Big) \\ & + \bar{\boldsymbol{\varepsilon}} : \Big( \frac{\partial \boldsymbol{q}^D}{\partial \Delta\boldsymbol{\varepsilon}^p_{(k)}} : \Delta\boldsymbol{\varepsilon}^p_{(k)} + \frac{\partial \boldsymbol{q}^D}{\partial \nabla\Delta\boldsymbol{\varepsilon}^p_{(k)}} \vdots \nabla\Delta\boldsymbol{\varepsilon}^p_{(k)} \Big) \\ & - \bar{\boldsymbol{\varepsilon}} : \boldsymbol{C}' : \Big( \boldsymbol{\varepsilon}(\Delta\boldsymbol{u}_{(k)}) - \Delta\boldsymbol{\varepsilon}^p_{(k)} \Big) \\ & + \nabla\bar{\boldsymbol{\varepsilon}} \vdots \Big( \frac{\partial \boldsymbol{m}^D}{\partial \Delta\boldsymbol{\varepsilon}^p_{(k)}} : \Delta\boldsymbol{\varepsilon}^p_{(k)} + \frac{\partial \boldsymbol{m}^D}{\partial \nabla\Delta\boldsymbol{\varepsilon}^p_{(k)}} \vdots \nabla\Delta\boldsymbol{\varepsilon}^p_{(k)} \Big) \\ & - \nabla\bar{\boldsymbol{\varepsilon}} \vdots \boldsymbol{A}' \vdots \Big( \nabla\boldsymbol{\varepsilon}(\Delta\boldsymbol{u}_{(k)}) - \nabla\Delta\boldsymbol{\varepsilon}^p_{(k)} \Big) \\ & + 2\mu L_e^2 \nabla\bar{\boldsymbol{\varepsilon}} \vdots \nabla\Delta\boldsymbol{\varepsilon}^p_{(k)} \Bigg) \mathrm{d}\mathcal{V}. \end{aligned} \tag{2.29}$$

Until the required convergence is achieved the displacements and plastic strains are updated by

$${}^{n+1}\boldsymbol{u}_{(k+1)} = {}^{n+1}\boldsymbol{u}_{(k)} + \Delta\boldsymbol{u}_{(k)}, \quad {}^{n+1}\boldsymbol{\varepsilon}^p_{(k+1)} = {}^{n+1}\boldsymbol{\varepsilon}^p_{(k)} + \Delta\boldsymbol{\varepsilon}^p_{(k)}. \tag{2.30}$$

**Remark 5.** Constitutive tensors $\boldsymbol{C}'$ and $\boldsymbol{A}'$ are, respectively, the deviatoric parts of the stiffness tensors $\boldsymbol{C}$ and $\boldsymbol{A}$, reflecting the fact that $\mathrm{tr}(\boldsymbol{\varepsilon}^p) = 0$. Unlike the classical isotropic case where $\boldsymbol{C}'$ can still be represented in a compact form as $\boldsymbol{C}' = 2\mu \boldsymbol{I}_{dev}$, in a general strain gradient isotropic case $\boldsymbol{A}'$ involves four out of five higher-order constants and takes rather complicated form. Hence, for generality and brevity, the deviatoric parts are not presented explicitly in the main body of the current paper.

## 3. Isogeometric discretization and numerical implementation

### 3.1. Isogeometric discretization

In IGA, for an isogeometric tensor product discretization of a 3D solution domain, first, a geometrical mapping between the 3D parameter space $[0, 1]^3$ and the problem domain $\mathcal{B}$ is defined by $\boldsymbol{x} : [0, 1]^3 \to \mathcal{B}$ as

$$\boldsymbol{x}(\xi, \eta, \zeta) = \sum_{i=1}^{n_\xi} \sum_{j=1}^{n_\eta} \sum_{k=1}^{n_\zeta} N_{i,j,k}^{p,q,r}(\xi, \eta, \zeta) \boldsymbol{X}_{i,j,k}. \tag{3.1}$$

Above, $\boldsymbol{X}_{i,j,k}$, $i = 1, \ldots, n_\xi$, $j = 1, \ldots, n_\eta$, $k = 1, \ldots, n_\zeta$, denote the control point coordinates, while the NURBS basis functions are defined as

$$N_{i,j,k}^{p,q,r}(\xi, \eta, \zeta) = \frac{P_{i,p}(\xi) Q_{j,q}(\eta) R_{k,r}(\zeta) \omega_{i,j,k}}{\sum_{\hat{i}=1}^{n_\xi} \sum_{\hat{j}=1}^{n_\eta} \sum_{\hat{k}=1}^{n_\zeta} P_{\hat{i},p}(\xi) Q_{\hat{j},q}(\eta) R_{\hat{k},r}(\zeta) \omega_{\hat{i},\hat{j},\hat{k}}}, \tag{3.2}$$

with $\xi$, $\eta$ and $\zeta$ denoting the coordinates of the parameter space and $\omega_{i,j,k}$, $i = 1, \ldots, n_\xi$, $j = 1, \ldots, n_\eta$, $k = 1, \ldots, n_\zeta$, standing for the weights associated with the NURBS control points. The B-spline basis functions $P_{i,p}$ of degree $p$ associated to the open knot vector $\Xi = \{0 = \xi_1, \xi_2, \ldots, \xi_{n_\xi + p + 1} = 1\}$ are defined as follows [77]:

$$P_{i,0}(\xi) = \begin{cases} 1, & \xi_i \le \xi < \xi_{i+1}, \\ 0, & \text{otherwise} \end{cases} \tag{3.3}$$

$$P_{i,p}(\xi) = \frac{\xi - \xi_i}{\xi_{i+p} - \xi_i} P_{i,p-1}(\xi) + \frac{\xi_{i+p+1} - \xi}{\xi_{i+p+1} - \xi_{i+1}} P_{i+1,p-1}(\xi). \tag{3.4}$$

The B-spline basis functions $Q_{j,q}$ and $R_{k,r}$ of degree $q$ and $r$, respectively, associated to the open knot vectors $H = \{0 = \eta_1, \eta_2, \ldots, \eta_{n_\eta + q + 1} = 1\}$ and $Z = \{0 = \zeta_1, \zeta_2, \ldots, \zeta_{n_\zeta + r + 1} = 1\}$, respectively, can be defined by following the same procedure.

### 3.2. Discrete formulation

Linearized problem of Section 2.3 is solved by conforming isogeometric Galerkin method formulated as follows: For ${}^{n+1}\boldsymbol{f} \in [L^2(\mathcal{B})]^3$ and ${}^{n+1}\boldsymbol{r} \in [L^2(\mathcal{B})]^6$, find $(\Delta \boldsymbol{u}_h, \Delta \boldsymbol{\varepsilon}_h^p) \in \boldsymbol{\mathcal{U}}_h \times \boldsymbol{\mathcal{E}}_h \subset \boldsymbol{\mathcal{U}} \times \boldsymbol{\mathcal{E}}$ such that

$$a^*(\Delta \boldsymbol{u}_h, \Delta \boldsymbol{\varepsilon}_h^p; \bar{\boldsymbol{u}}, \bar{\boldsymbol{\varepsilon}}) = l(\bar{\boldsymbol{u}}, \bar{\boldsymbol{\varepsilon}}) - a({}^{n+1}\boldsymbol{u}_h, {}^{n+1}\boldsymbol{\varepsilon}_h^p; \bar{\boldsymbol{u}}, \bar{\boldsymbol{\varepsilon}}), \tag{3.5}$$

$\forall (\bar{\boldsymbol{u}}, \bar{\boldsymbol{\varepsilon}}) \in \bar{\boldsymbol{\mathcal{U}}}_h \times \bar{\boldsymbol{\mathcal{E}}}_h \subset \bar{\boldsymbol{\mathcal{U}}} \times \bar{\boldsymbol{\mathcal{E}}}$. Subscript $(k)$ is omitted here for brevity.

The corresponding isoparametric discrete space for the approximation of, respectively, the displacement and plastic strain fields

$$\Delta \boldsymbol{u}_h(\xi, \eta, \zeta) = \sum_{i=1}^{n_\xi} \sum_{j=1}^{n_\eta} \sum_{k=1}^{n_\zeta} N_{i,j,k}^{p,q,r}(\xi, \eta, \zeta) \Delta \boldsymbol{U}_{i,j,k}, \tag{3.6}$$

$$\Delta \boldsymbol{\varepsilon}_h^p(\xi, \eta, \zeta) = \sum_{i=1}^{n_\xi} \sum_{j=1}^{n_\eta} \sum_{k=1}^{n_\zeta} N_{i,j,k}^{p,q,r}(\xi, \eta, \zeta) \Delta \boldsymbol{E}_{i,j,k}^p \tag{3.7}$$

is defined such that $\Delta \boldsymbol{u}_h \in [S_h]^3$ and $\Delta \boldsymbol{\varepsilon}_h^p \in [S_h]^6$ with unknown increments of the control variables $\Delta \boldsymbol{U}_{i,j,k}$ and $\Delta \boldsymbol{E}_{i,j,k}^p$, where $S_h = \{N_{i,j,k}^{p,q,r} \circ \boldsymbol{x}^{-1}\}$.

The tensor product mesh of the isogeometric NURBS discretization of the solid volume is defined as (cf. [86,88] for 2D discretizations)

$$\mathcal{T}_h = \{K = \boldsymbol{x}([\hat{\xi}_i, \hat{\xi}_{i+1}] \times [\hat{\eta}_j, \hat{\eta}_{j+1}] \times [\hat{\zeta}_k, \hat{\zeta}_{k+1}])\}, \tag{3.8}$$

with $1 \leq i \leq n_p - 1$, $1 \leq j \leq n_q - 1$ and $1 \leq k \leq n_r - 1$, where $\hat{\Xi} = \{0 = \hat{\xi}_1, \ldots, \hat{\xi}_{n_p} = 1\}$, $\hat{H} = \{0 = \hat{\eta}_1, \ldots, \hat{\eta}_{n_q} = 1\}$ and $\hat{Z} = \{0 = \hat{\zeta}_1, \ldots, \hat{\zeta}_{n_r} = 1\}$ are the modified knot vectors containing the non-repeated knot values of $\Xi$, $H$ and $Z$, respectively, with $n_p$, $n_q$ and $n_r$ denoting the number of knots without repetition in the respective directions. The mesh size $h = \max_{K \in \mathcal{T}_h} h_K$ serves as the mesh index, as usual, with $h_K = \mathrm{diam}(K)$.

By assuming global regularity $C^{s-1}$ ($s = \min(p, q, r)$) over $\mathcal{T}_h$, with $s \geq 2$, it holds that $S_h \subset H^2(\mathcal{B})$, which provides a conforming and consistent Galerkin method formulated in (3.5) with $\boldsymbol{\mathcal{U}}_h = [S_h]^3 \cap \boldsymbol{\mathcal{U}}$, $\hat{\boldsymbol{\mathcal{U}}}_h = [S_h]^3 \cap \hat{\boldsymbol{\mathcal{U}}}$, and $\boldsymbol{\mathcal{E}}_h = [S_h]^6 \cap \boldsymbol{\mathcal{E}}$, $\hat{\boldsymbol{\mathcal{E}}}_h = [S_h]^6 \cap \hat{\boldsymbol{\mathcal{E}}}$.

**Remark 6.** Numerical realization of method formulated in Section 3.2 is limited to geometries with single patch representation due to higher-order continuity restrictions across patch boundaries. Analysis-suitable multi-patch parametrizations for 3D $C^1$ isogeometric spaces are required (see [113,114] for analysis-suitable $G^1$ planar multi-patch parametrizations).

### 3.3. Numerical implementation

The strain gradient elasto-plasticity material model addressed in Section 2 and the corresponding isogeometric Galerkin methods are implemented in a robust, backward Euler finite element framework as user element subroutines of the commercial FE software Abaqus. The implementation steps are given next in a matrix form using Voigt notation. Vectors and matrices are denoted, respectively, by single and double underline.

The trial functions approximations are introduced in the form

$$\underline{u}_h = \underline{\underline{N}}^u \underline{\hat{u}}, \quad \underline{\varepsilon}^p_h = \underline{\underline{N}}\, \underline{\hat{\varepsilon}}^p, \tag{3.9}$$

where the column vectors of unknown control point displacements and plastic strains are represented as

$$\underline{\hat{u}} = \left[\underline{\hat{u}}^{(1)} \quad \ldots \quad \underline{\hat{u}}^{(n)}\right]^T, \quad \underline{\hat{\varepsilon}}^p = \left[\underline{\hat{\varepsilon}}^{p(1)} \quad \ldots \quad \underline{\hat{\varepsilon}}^{p(n)}\right]^T. \tag{3.10}$$

For the $i$th control point, displacements and plastic strains are written as

$$\underline{\hat{u}}^{(i)} = \left[\hat{u}^{(i)}_x \; \hat{u}^{(i)}_y \; \hat{u}^{(i)}_z\right], \quad \underline{\hat{\varepsilon}}^{p(i)} = \left[\hat{\varepsilon}^{p\,(i)}_{xx} \; \hat{\varepsilon}^{p\,(i)}_{yy} \; \hat{\varepsilon}^{p\,(i)}_{zz} \; \hat{\gamma}^{p\,(i)}_{yz} \; \hat{\gamma}^{p\,(i)}_{xz} \; \hat{\gamma}^{p\,(i)}_{xy}\right], \tag{3.11}$$

with $i = 1, \ldots, n$ and $n$ being a total number of control points. The total strain, total and plastic strain gradients are approximated, respectively, as

$$\underline{\varepsilon}_h = \underline{\underline{B}}\, \underline{\hat{u}}, \quad \underline{\nabla\varepsilon}_h = \underline{\underline{L}}\, \underline{\hat{u}}, \quad \underline{\nabla\varepsilon}^p_h = \underline{\underline{M}}\, \underline{\hat{\varepsilon}}^p. \tag{3.12}$$

Matrices $\underline{\underline{N}}^u$ and $\underline{\underline{N}}$ composed of the basis functions as well as matrices $\underline{\underline{B}}$, $\underline{\underline{L}}$ and $\underline{\underline{M}}$ containing the derivatives of the basis functions are explicitly presented in Appendix A (the derivative details for the two-dimensional case can be found in [81], for instance).

Substituting the trial functions approximations (3.9) in (2.28) and introducing the test functions approximations similar to (3.9), we rewrite the linearized problem of Section 2.3 in a discretized form as

$$\delta\underline{V}^T \underline{\underline{K}} \Delta\underline{U} = -\delta\underline{V}^T \underline{R}, \tag{3.13}$$

where $\underline{\underline{K}}$ denotes the total stiffness matrix of the problem, $\underline{R}$ is the complete vector of residual forces, $\Delta\underline{U}$ stands for the total vector of unknown variable increments and $\delta\underline{V}$ is the vector of virtual variables. Because the vector of virtual variables is arbitrary, a discretized Newton–Raphson scheme can be formulated in the following form

$$\underline{\underline{K}} \Delta\underline{U}_{(k)} = -{}^{n+1}\underline{R}_{(k)}, \quad {}^{n+1}\underline{U}_{(k+1)} = {}^{n+1}\underline{U}_{(k)} + \Delta\underline{U}_{(k)}, \tag{3.14}$$

where the stiffness matrix, residual force vector and vector of unknown variables are split as

$$\underline{\underline{K}} = \begin{bmatrix} \underline{\underline{K}}_{u,u} & \underline{\underline{K}}_{u,\varepsilon^p} \\ \underline{\underline{K}}_{\varepsilon^p,u} & \underline{\underline{K}}_{\varepsilon^p,\varepsilon^p} \end{bmatrix}, \quad \underline{R} = \begin{bmatrix} \underline{R}_u \\ \underline{R}_{\varepsilon^p} \end{bmatrix}, \quad \underline{U} = \begin{bmatrix} \underline{\hat{u}} \\ \underline{\hat{\varepsilon}}^p \end{bmatrix}. \tag{3.15}$$

Here and in what follows, superscript $n+1$ and subscripts $(k)$, $(k+1)$ and $h$ are dropped for sake of brevity.

In order to assure the second-order convergence of the Newton–Raphson scheme, the submatrices of the consistent total stiffness matrix are derived as follows

$$\underline{\underline{K}}_{u,u} = \int_{\mathcal{B}} \left( \underline{\underline{B}}^T \underline{\underline{C}} \, \underline{\underline{B}} + \underline{\underline{L}}^T \underline{\underline{A}} \, \underline{\underline{L}} \right) \mathrm{d}\mathcal{V}, \tag{3.16}$$

$$\underline{\underline{K}}_{u,\varepsilon^p} = -\int_{\mathcal{B}} \left( \underline{\underline{B}}^T \underline{\underline{C}}' \, \underline{\underline{N}} + \underline{\underline{L}}^T \underline{\underline{A}}' \, \underline{\underline{M}} \right) \mathrm{d}\mathcal{V}, \tag{3.17}$$

$$\underline{\underline{K}}_{\varepsilon^p,u} = -\int_{\mathcal{B}} \left( \underline{\underline{N}}^T \underline{\underline{C}}' \, \underline{\underline{B}} + \underline{\underline{M}}^T \underline{\underline{A}}' \, \underline{\underline{L}} \right) \mathrm{d}\mathcal{V}, \tag{3.18}$$

$$\begin{aligned} \underline{\underline{K}}_{\varepsilon^p,\varepsilon^p} = \int_{\mathcal{B}} \Bigg( & \underline{\underline{N}}^T \left[ \left( \frac{\partial \underline{q}^D}{\partial \Delta \underline{\varepsilon}^p} + \underline{\underline{C}}' \right) \underline{\underline{N}} + \frac{\partial \underline{q}^D}{\partial \Delta \underline{\nabla \varepsilon}^p} \underline{\underline{M}} \right] \\ & + \underline{\underline{M}}^T \left[ \left( \frac{\partial \underline{m}^D}{\partial \Delta \underline{\nabla \varepsilon}^p} + 2\mu L_e^2 \underline{\underline{H}}_{\nabla\varepsilon} + \underline{\underline{A}}' \right) \underline{\underline{M}} + \frac{\partial \underline{m}^D}{\partial \Delta \underline{\varepsilon}^p} \underline{\underline{N}} \right] \Bigg) \mathrm{d}\mathcal{V}. \end{aligned} \tag{3.19}$$

Derivative details for integrands of (3.19) are given in Appendix A. The subvectors of residual forces appear in the form

$$\underline{R}_u = \int_{\mathcal{B}} \left( \underline{\underline{B}}^T \underline{\sigma} + \underline{\underline{L}}^T \underline{\tau} \right) \mathrm{d}\mathcal{V}, \tag{3.20}$$

$$\underline{R}_{\varepsilon^p} = \int_{\mathcal{B}} \left( \underline{\underline{N}}^T \left( \underline{q} - \underline{\sigma}' \right) + \underline{\underline{M}}^T \left( \underline{m} - \underline{\tau}' \right) \right) \mathrm{d}\mathcal{V}, \tag{3.21}$$

where only internal forces are presented for brevity.

The Cauchy stress, double stress and energetic moment stress quantities are defined at the end of the current time increment, respectively, through the total and plastic strains and their gradients in the form

$$\underline{\sigma} = \underline{\underline{C}} \, \underline{\varepsilon} - \underline{\underline{C}}' \underline{\varepsilon}^p, \quad \underline{\tau} = \underline{\underline{A}} \, \underline{\nabla \varepsilon} - \underline{\underline{A}}' \underline{\nabla \varepsilon}^p, \quad \underline{m}^E = 2\mu L_e^2 \underline{\underline{H}}_{\nabla\varepsilon} \underline{\nabla \varepsilon}^p. \tag{3.22}$$

Deviatoric parts of the Cauchy and double stress vectors are written as

$$\underline{\sigma}' = \underline{\underline{C}}' (\underline{\varepsilon}' - \underline{\varepsilon}^p), \quad \underline{\tau}' = \underline{\underline{A}}' (\underline{\nabla \varepsilon}' - \underline{\nabla \varepsilon}^p), \tag{3.23}$$

where $\underline{\varepsilon}'$ stands for deviatoric part of the total strain vector.

Dissipative stresses introduced in (2.21) take the following vector form

$$\underline{q}^D = \frac{2}{3} \frac{\Sigma}{\Delta E^p} \underline{\underline{H}}_{\varepsilon} \Delta \underline{\varepsilon}^p, \quad \underline{m}^D = L_p^2 \frac{\Sigma}{\Delta E^p} \underline{\underline{H}}_{\nabla\varepsilon} \Delta \underline{\nabla \varepsilon}^p, \tag{3.24}$$

where the increments of the scalar and vectorial field variables within the time step $\Delta t$ are defined as

$$\Delta E^p = \dot{E}^p \Delta t, \quad \Delta \underline{\varepsilon}^p = \dot{\underline{\varepsilon}}^p \Delta t, \quad \Delta \underline{\nabla \varepsilon}^p = \underline{\nabla \dot{\varepsilon}}^p \Delta t. \tag{3.25}$$

Matrices of elastic constants $\underline{\underline{C}}$, $\underline{\underline{C}}'$, $\underline{\underline{A}}$ and $\underline{\underline{A}}'$ as well as diagonal matrices $\underline{\underline{H}}_{\varepsilon}$ and $\underline{\underline{H}}_{\nabla\varepsilon}$ which provide a transition from tensorial to Voigt notation are specified in Appendix A.

As gradient plasticity theories are commonly implemented in a rate-dependent framework, an effective flow resistance $\Sigma$ involves the most exploited viscoplastic function $V$ in the form of power-law (see [55,115])

$$\Sigma(E^p, \dot{E}^p) = \sigma_y(E^p) V(\dot{E}^p), \quad V(\dot{E}^p) = \left( \frac{\dot{E}^p}{\dot{\varepsilon}_0} \right)^m, \tag{3.26}$$

where $\sigma_y$ denotes the current flow stress, $\dot{\varepsilon}_0$ and $m$ stand, respectively, for the reference strain rate and viscoplastic (or rate sensitivity) exponent. However, with this choice of the viscoplastic flow expression, some numerical issues arise leading to ill-conditioned finite element systems. To overcome the issues, some regularization techniques have been developed in [62,63,65]. The recent algorithm, proposed in [65], is utilized in our work (see details in Appendix B). For the flow stress, a Johnson–Cook hardening law [116] is employed

$$\sigma_y(E^p) = \sigma_0 + K (E^p)^N, \tag{3.27}$$

where $\sigma_0$ is initial yield stress, $K$ and $N$ stand, respectively, for the hardening modulus and hardening exponent.

## 4. Numerical results

In this section, we provide convergence analyses and parameter study by considering four benchmarks, namely shear and bending of a strip, stretching of a plate with a hole and torsion of a brick problems. For the first two problems, we verify the isogeometric implementation by comparing the results with the implementation based on $C^0$ 8-node biquadratic plane strain finite elements [64] (source files are available on www.empaneda.com/codes). The present isogeometric implementation is based on full Gauss integration scheme (see [117,118] for alternative reduced quadrature techniques).

Classical elasto-plastic material characteristics are chosen as follows: $E = 200$ GPa, $\nu = 0.3$, $\sigma_0 = 200$ MPa, $K = 500$ MPa and $N = 0.5$. Within the rate-dependent framework, the reference strain rate and viscoplastic exponent are set, respectively, to $\dot{\varepsilon}_0 = 0.01$ s$^{-1}$ and $m = 0.1$. The effect of viscoplastic exponent $m$ is also studied and transition to the rate-independent case is demonstrated. Built-in Abaqus (conventional) Johnson–Cook plasticity model (see details in Abaqus Analysis User's Manual [119]) is utilized for producing rate-independent reference solutions.

Regarding the higher-order material moduli, determination of length scale parameters still remains an ongoing research topic (see remarks in Section 6). In [120], performing Molecular Statics calculations of stress in a body-centered cubic Fe crystal, a material characteristic (single) length scale parameter was estimated to be $0.46a$, where $a$ is the lattice parameter describing a unit cell. In [32], for 3D cellular plate-like structures with a triangular (extruded lattice) microarchitecture (with relative density 34.6%), a set of four length scale parameters (shown to be a minimum number of independent parameters required for describing a bending state of the cellular plate-like structures) are estimated to be within a range from $0.2b$ to $0.38b$, where $b$ denotes the height of a triangular unit cell. This provides some estimation of a possible range for the material characteristic length scales. Hence, within this section, ratio of geometric characteristics, e.g., a strip height in Section 4.1, to the length scale parameters does not drop below value 3. However, for the problem in Section 4.3, namely stretching of a plate with a hole, we made an exception and allowed the hole radius to be as small as two elastic length scale parameters. This is made intentionally in order to clearly show an effect of the elastic length scale on stress distribution.

### 4.1. Shear of a long strip

As a first benchmark, let us consider a simple shear (in the $x$-direction) of a long strip. The strip has height $H$ in the $y$-direction. The bottom surface ($y = 0$) is clamped ($u_x = u_y = 0$). At the top surface ($y = H$) normal displacement is constrained ($u_y = 0$) and either displacement or traction is applied in the $x$-direction. Zero plastic strains ($\varepsilon^p_{xx} = \varepsilon^p_{yy} = \gamma^p_{xy} = 0$) are imposed at the top ($y = H$) and bottom ($y = 0$) surfaces, modelling dislocations piling-up. For the given boundary conditions the shear problem is considered to be one-dimensional with only $u_x(y)$ and $\gamma^p_{xy}(y)$ active kinematical variables.

The strip shear is modelled using a single column of 3D elements (knot spans). The side surfaces (with normals along the $x$- and $z$-directions) are subjected to the boundary conditions $u_y = u_z = 0$ and $\varepsilon^p_{xx} = \varepsilon^p_{yy} = \varepsilon^p_{zz} = \gamma^p_{xz} = \gamma^p_{yz} = 0$. Traction force $T_x = 3$ GPa is applied to the top surface. In the height direction, the domain is discretized with B-splines of degree $q$ and $C^{q-1}$ global continuity. Whereas in the $x$- and $z$-directions, a linear interpolation is considered to be sufficient since (for a given geometry and boundary conditions) the displacement and plastic strain fields being a problem solution change only in the height direction, i.e., $y$-direction. The dissipative and energetic length scale parameter values are set in this study to $L_p = L_e = H/4$. The elastic length scale parameter equals to $L_g = 0$ (SGP model) and $L_g = H/4$ (SGEP model). In terms of the microstructure it means that there are, for instance, one or two unit cells of crystal or metamaterial lattice in the height direction. Within the SGEP model, additional boundary condition, namely zero normal derivative of the displacement field ($\partial u_x/\partial y = 0$), is prescribed on the top and bottom surfaces (example addressing prescription of the higher-order boundary conditions is considered in [121] for square lattice structures). Following the Abaqus nomenclature, results using $C^0$ 8-node biquadratic plane strain finite elements are denoted by CPE8 (continuum plane strain 8-node elements).

Figs. 4.1–4.3, within SGP (left) and SGEP (right) models, show the convergence of, respectively, the displacement, shear strain and equivalent plastic strain for the different polynomial orders. In Fig. 4.1, the converged solution is $u_x(H)/H = 0.08567$ (SGP model) and $u_x(H)/H = 0.06687$ (SGEP model). For polynomial orders $q \geq 3$ the convergence is quite fast. For quartic and quintic basis functions the converged solution (with respect to displacement) is obtained already with 1 (SGP model) and 2 (SGEP model) knot spans. For quadratic shape

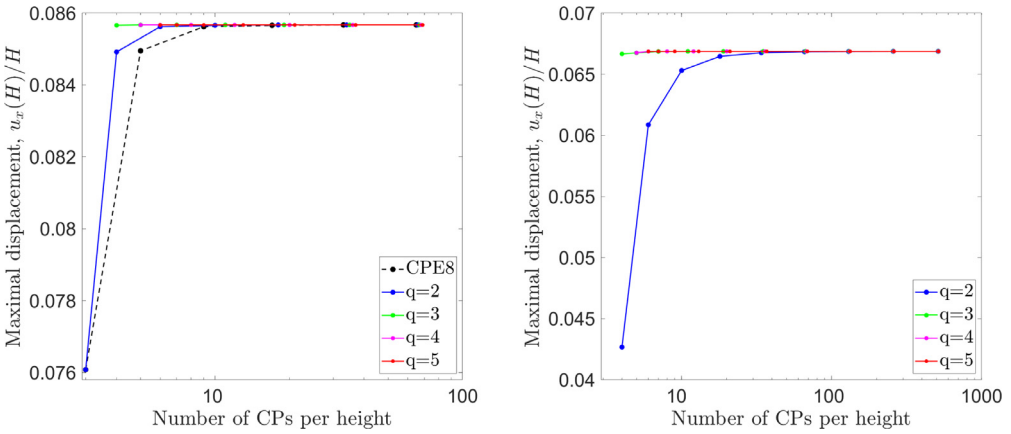


**Fig. 4.1.** Shear of a constrained strip. Convergence of the maximal displacement ($u_x(H)$) normalized by the strip height for $L_g = 0$ (left) and $L_g = H/4$ (right). $q$ stands for the B-Spline degree within IGA. CPE8 indicates the results using 8-node biquadratic plane strain finite elements. (For interpretation of the references to colour in this figure legend, the reader is referred to the web version of this article.)

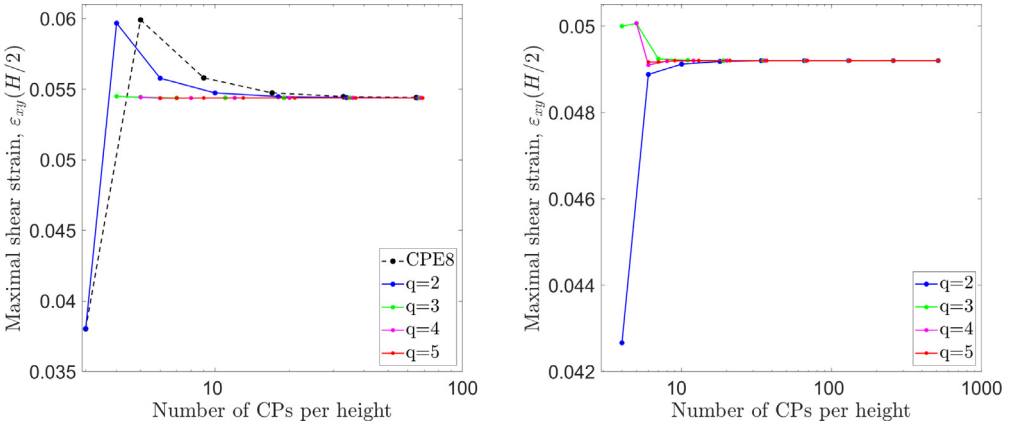


**Fig. 4.2.** Shear of a constrained strip. Convergence of the maximal shear strain ($\varepsilon_{xy}(H/2)$) for $L_g = 0$ (left) and $L_g = H/4$ (right). $q$ stands for the B-Spline degree within IGA. CPE8 indicates the results using 8-node biquadratic plane strain finite elements. (For interpretation of the references to colour in this figure legend, the reader is referred to the web version of this article.)

functions, the convergence within SGEP model is slower comparing to SGP model requiring, respectively, 256 and 16 knot spans to obtain the converged solution.

In Fig. 4.2, the converged solution is $\varepsilon_{xy}(H/2) = 0.05439$ (SGP model) and $\varepsilon_{xy}(H/2) = 0.04920$ (SGEP model). For quadratic shape functions, the situation is opposite as in Fig. 4.1. The convergence within SGP model is slower comparing to SGEP model requiring, respectively, 64 and 16 knot spans to obtain the converged solution. For polynomial orders $q \geq 3$ the convergence is quite fast. Within both SGP and SGEP models, for cubic basis functions, the converged solution (with respect to shear strain) is obtained with 8 knot spans, while for quartic and quintic basis functions — with 4 knot spans.

Regarding the plastic strain, the SGP and SGEP models provide identical solutions. Indeed, by integrating first equation in (2.9) and fulfilling boundary conditions corresponding to applied traction forces $T_x$, it can be seen that for 1D (shear) problem the second equation transforms to $q_{xy} - \partial_y m_{xy} = T_x$ within both models, which shows that plastic strain is not affected by the gradient-elastic part. In Fig. 4.3, the converged solution is $E^p(H) = 0.05027$ (for both SGP and SGEP models). For quadratic shape functions, the convergence is quite slow. For polynomial orders $q \geq 3$, the convergence is improved and for quintic basis functions the converged solution is obtained already with 8 knot spans (within both SGP and SGEP models).

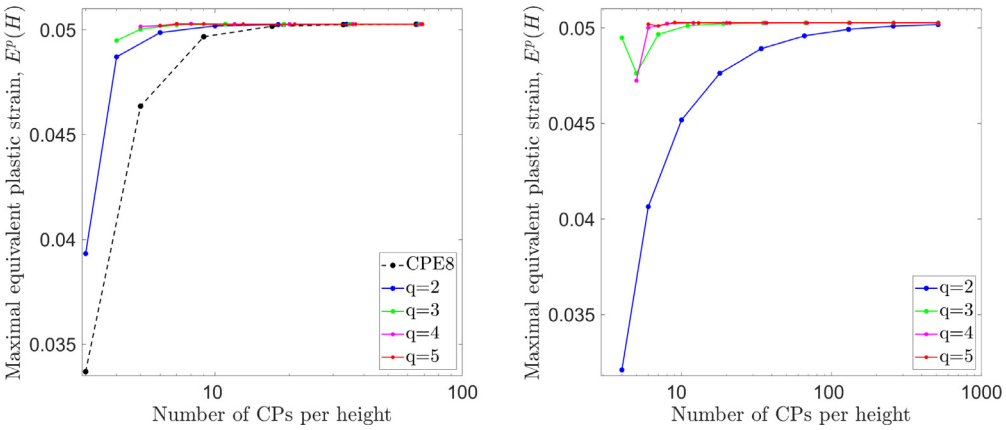


**Fig. 4.3.** Shear of a constrained strip. Convergence of the maximal equivalent plastic strain ($E^p(0)$ or $E^p(H)$) for $L_g = 0$ (left) and $L_g = H/4$ (right). $q$ stands for the B-Spline degree within IGA. CPE8 indicates the results using 8-node biquadratic plane strain finite elements. (For interpretation of the references to colour in this figure legend, the reader is referred to the web version of this article.)

A comment should be given regarding nonmonotonic behaviour in the plotted convergence results (for first few dots) with labels $q = 3$, $q = 4$ and $q = 5$ in Figs. 4.2 and 4.3 (right). It might be caused by the way how the higher-order essential boundary condition ($\partial u_x/\partial y = 0$) is prescribed on the top and bottom surfaces. Because of the tensor product nature of a B-Spline solid construction (see Section 3.1) and the fact that a B-Spline curve with an open knot vector is tangential to its control polygon at the start and the end of the curve, fixing the $x$-component of the second layer (in the $xz$-plane) of control points keeps the tangent at the bottom surface fixed, which automatically fulfils condition $\partial u_x/\partial y = 0$ at $y = 0$. The same procedure holds for the top surface. This approach reduces the number of basis functions and active (displacement) degrees of freedom involved in the calculations, which has a significant effect for meshes with only one finite element (knot span). However, the observed nonmonotonic behaviour does not hold in case of the quadratic functions, which might be related to the restrictions applied to initial discretization. The described procedure implies minimum four control points in the height direction which is possible only for meshes with at least two elements. Hence, the starting point for curves with label $q = 2$ corresponds to the mesh with two elements, unlike curves with labels $q = 3$, $q = 4$ and $q = 5$, where the starting points correspond to the meshes with one element.

Next, for mesh of 32 elements (knot spans) in the height direction with B-Splines of degree 5 providing $C^4$ global continuity, Figs. 4.4–4.7 demonstrate material response for different values of the elastic, dissipative and energetic length scale parameters. Displacement $u_x(H) = 0.08H$ with loading rate $\dot{u}_x/H = 0.005$ s$^{-1}$ is prescribed on the top surface. Solid, dotted and dashed lines represent a variation in the dissipative length scale parameter with values set, respectively, to $L_p = H/100$, $L_p = H/8$ and $L_p = H/4$. Black, blue and red colours are utilized to reflect a change in the elastic length scale parameter values from $L_g = 0$ to $L_g = H/4$. From left to right, results correspond to the energetic length scale parameter taken with values $L_e = H/100$, $L_e = H/8$ and $L_e = H/4$.

In Fig. 4.4, traction (or reaction) force $T_x$ normalized by $\sigma_0/\sqrt{3}$ at $y = H$ is plotted against normalized applied displacement, where curves are displayed only for $u_x(H)/H = 0.005$. For $L_g = 0$, the black curves show the results within SGP model. It can be clearly seen that the dissipative and energetic length scales are responsible for, respectively, dissipative (yield) strengthening and energetic hardening [20]. When the elastic length scale comes into play, the SGEP model demonstrates its capability of capturing materials stiffening phenomenon. This is reflected by the increase in the slope of the elastic part of the curves when the sample size is comparable with the materials elastic length scale. It can also be observed that the elasticity-related length scale parameter, on the one hand, significantly influences the hardening (level of the curves after yielding point) when the energetic length scale parameter is active and of the same magnitude as the elastic one. On the other hand, the effect is minor when the energetic length scale is negligible. Regarding materials (yield) strengthening phenomenon, there is no significant effect from gradient-elastic part of the SGEP model.

Distributions of the total shear strain, plastic shear strain and equivalent plastic strain fields along the strip height are plotted, respectively, in Figs. 4.5, 4.6 and 4.7. For cases when the energetic length scale is relatively

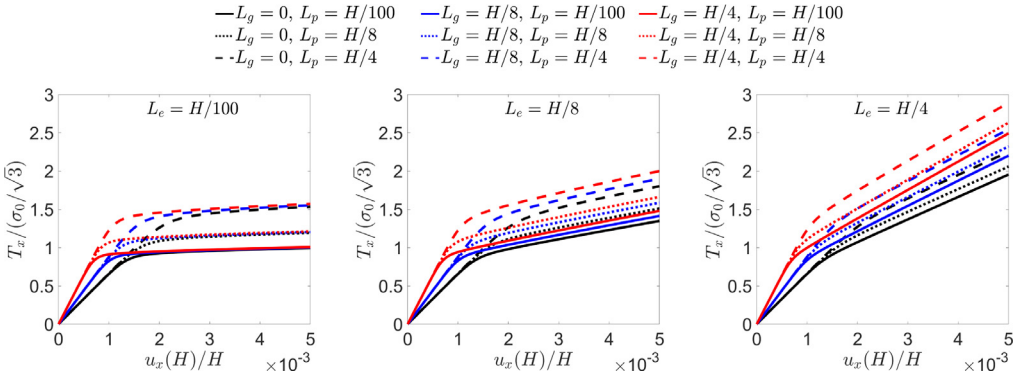


**Fig. 4.4.** Shear of a constrained strip. Normalized traction force versus normalized displacement at the strip top surface for $L_e = H/100$ (left), $L_e = H/8$ (middle) and $L_e = H/4$ (right). (For interpretation of the references to colour in this figure legend, the reader is referred to the web version of this article.)

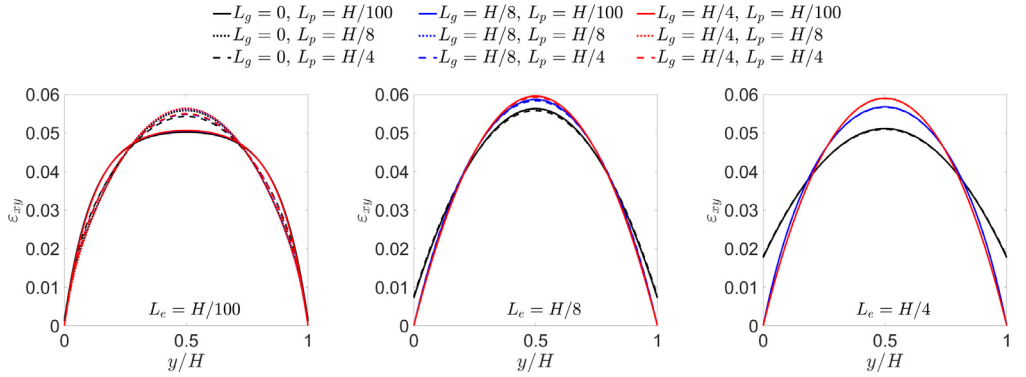


**Fig. 4.5.** Shear of a constrained strip. Distribution of the total shear strain field along the strip height for $L_e = H/100$ (left), $L_e = H/8$ (middle) and $L_e = H/4$ (right). (For interpretation of the references to colour in this figure legend, the reader is referred to the web version of this article.)

small ($L_e = H/100$), it can be seen that the curves are grouped by attribute of the lines type. This means that the elastic length scale brings minor contribution and the strains profile is mainly affected by the dissipative length scale. When the energetic length scale increases (or the sample size decreases), the attribute changes and the curves are grouped with respect to the lines colour. For total and plastic shear strains in Figs. 4.5 and 4.6 ($L_e = H/4$), the solid, dotted and dashed lines of the same colour are almost indistinguishable, which indicates that the strain profiles are mainly affected by the elastic rather than the dissipative length scale. Regarding the equivalent plastic strain, due to the presence of plastic strain gradients in (2.20), there is a qualitative and quantitative change of the strain profiles in the vicinity of the strip surfaces. It can be seen that as long as the energetic length scale increases the effect of the dissipative length scale decreases but remains strong. At the same time, the elastic length scale affects the magnitude of strain profiles.

Influence of the viscoplastic exponent $m$ is presented in Fig. 4.8 (left). Results correspond to a classical plasticity model, i.e., all length scale parameters are set to zero. Shear plastic strains are released on the top and bottom surfaces. Abaqus built-in rate-independent Johnson–Cook plasticity model (see details in Abaqus Analysis User's Manual [119]) provides a reference curve. It can be seen that the rate-independent material response is retrieved as the viscoplastic exponent tends to zero. For $m = 0.001$, the red dots lie almost exactly on the black curve.

### *4.2. Bending of a thin strip*

Next, we consider a bending problem of a strip. The strip has length $L$ in the $x$-direction and thickness $H$ in the $y$-direction. Length to thickness ratio is set to $L/H = 4$. The bottom ($y = 0$) and top ($y = H$) surfaces

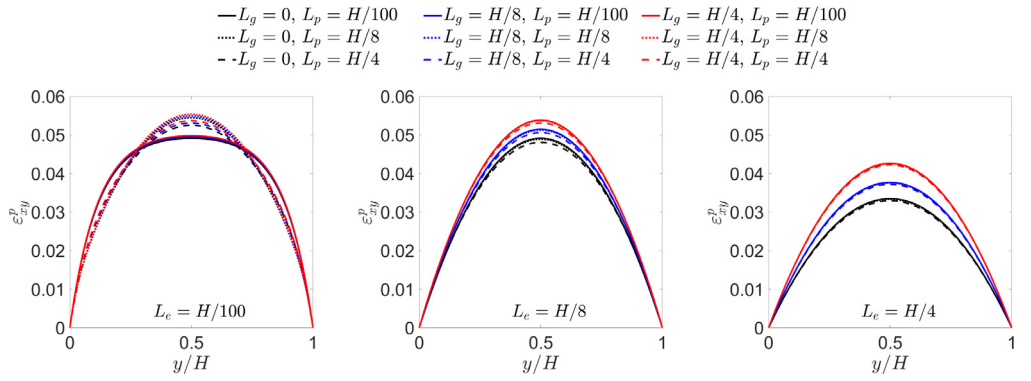


**Fig. 4.6.** Shear of a constrained strip. Distribution of the plastic shear strain field along the strip height for $L_e = H/100$ (left), $L_e = H/8$ (middle) and $L_e = H/4$ (right). (For interpretation of the references to colour in this figure legend, the reader is referred to the web version of this article.)

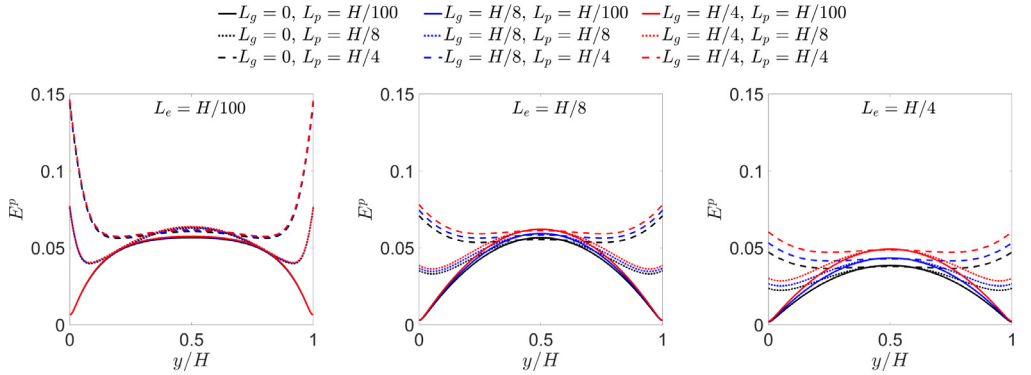


**Fig. 4.7.** Shear of a constrained strip. Distribution of the equivalent plastic strain field along the strip height for $L_e = H/100$ (left), $L_e = H/8$ (middle) and $L_e = H/4$ (right). (For interpretation of the references to colour in this figure legend, the reader is referred to the web version of this article.)

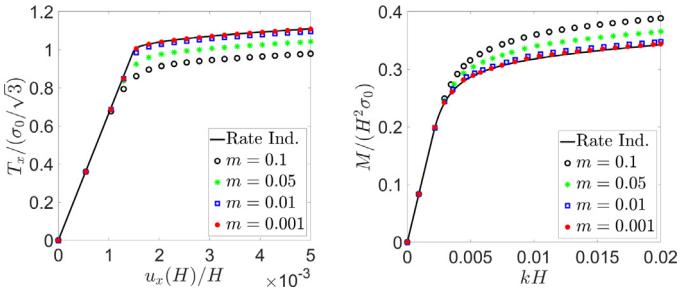


**Fig. 4.8.** Influence of the viscoplastic exponent $m$ on the material response curves for $L_g = L_p = L_e = 0$. Left: Normalized traction force versus normalized displacement at the strip top surface for shear problem. Right: Normalized bending moment versus normalized curvature for bending problem. Black solid line represents the solution obtained within conventional rate-independent plasticity model. (For interpretation of the references to colour in this figure legend, the reader is referred to the web version of this article.)

are subjected to homogeneous natural boundary conditions. The strip ends ($x = 0$ and $x = L$) have longitudinal displacement component governed by the constraint $u_x = \pm k(y - H/2)L/2$ at $x = 0, L$ and traction-free conditions in the thickness direction. In the constraining expression, by analogy with the classical case, $k$ is called a bending curvature. Either displacement or traction is applied at corners ($x = 0$, $y = 0$) and ($x = L$, $y = 0$) in the $x$-direction. The problem is considered to be two dimensional.

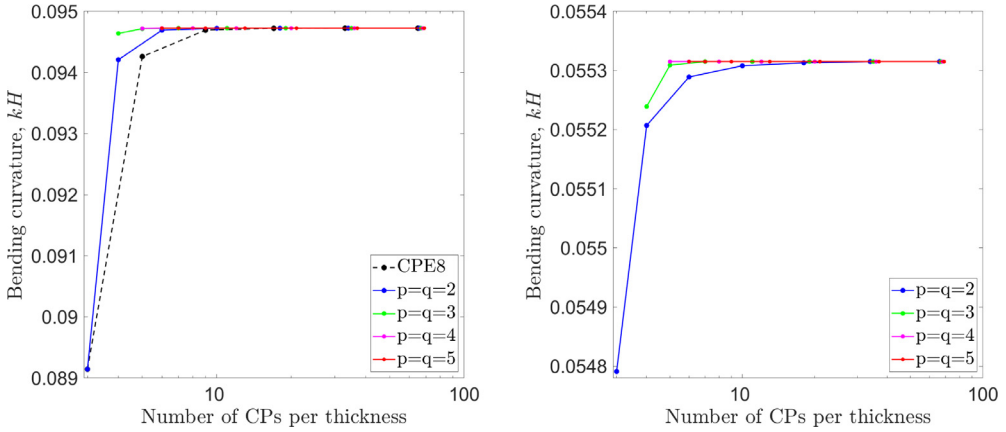


**Fig. 4.9.** Bending of a strip. Convergence of the bending curvature $kH = 4u_x(0, H)/L$ for $L_g = 0$ (left) and $L_g = H/3$ (right). $p$ and $q$ stand for the B-Spline degree within IGA. CPE8 indicates the results using 8-node biquadratic plane strain finite elements. (For interpretation of the references to colour in this figure legend, the reader is referred to the web version of this article.)

The strip bending problem is modelled by $N_e \times N_e \times 1$ 3D elements (knot spans). The side surfaces (with normals along the $z$-direction) are subjected to zero normal displacements $u_z = 0$. Edge force resulting in the bending moment per unit width $M = 1100$ N is applied to edges $(x = 0,\ y = 0)$ and $(x = L,\ y = 0)$ in the $x$-direction. B-splines of degree $p = q$ and $C^{p-1}$ global continuity are utilized in the $x$- and $y$-directions, while linear interpolation is used in the $z$-direction. This is considered to be sufficient since (for a given geometry and boundary conditions) the displacement and plastic strain fields being a problem solution do not vary in the $z$-direction. The dissipative and energetic length scale parameter values are set in this study to $L_p = L_e = H/3$. The elastic length scale parameter equals to $L_g = 0$ (SGP model) and $L_g = H/3$ (SGEP model). In terms of the microstructure, case when $L_g = H/3$ corresponds, for instance, to bending of trusses made of one unit cell of triangular lattice in the thickness direction [29].

Figs. 4.9–4.11, within SGP (left) and SGEP (right) models, show the convergence of, respectively, the bending curvature, maximal tensile strain and maximal equivalent plastic strain for the different polynomial orders. In Fig. 4.9, the converged solution is $kH = 0.09472$ (SGP model) and $kH = 0.05532$ (SGEP model). For polynomial orders $q \geq 3$ the convergence is quite fast. For quartic and quintic basis functions, the converged solution (with respect to bending curvature) is obtained already with 1 knot span (within both models). For quadratic shape functions, the convergence is slower requiring 8 (SGP model) and 32 (SGEP model) knot spans to obtain the converged solution.

In Fig. 4.10, the converged solution is $\varepsilon_{xx}(L/2, 0) = 0.04736$ (SGP model) and $\varepsilon_{xx}(L/2, 0) = 0.02766$ (SGEP model). For polynomial orders $q \geq 3$ the convergence is quite fast. For quintic basis functions, the converged solution is obtained already with 1 knot span (within both models). In Fig. 4.11, the converged solution is $E^p(L/2, H/2) = 0.01946$ (SGP model) and $E^p(L/2, 0) = 0.01920$ (SGEP model). For polynomial orders $q \geq 3$, the convergence is quite fast and for quintic basis functions the converged solution is obtained already with 1 (SGP model) and 2 (SGEP model) knot spans. For quadratic shape functions, the convergence is slower requiring 64 (SGP model) and 128 (SGEP model) knot spans to obtain the converged solution.

Next, the strip domain is discretized by $8 \times 8 \times 1$ elements (knot spans) with B-Splines of degree 5 providing $C^4$ global continuity. Figs. 4.12–4.14 present material response for different values of the elastic, dissipative and energetic length scale parameters. The strip is bent by applying displacements $u_x(0, H) = 0.1H$ and $u_x(L, H) = -0.1H$ at the strip corners with loading rate $\dot{u}_x/H = 0.1\ \text{s}^{-1}$. Solid, dotted and dashed lines represent a variation in the dissipative length scale parameter with values set, respectively, to $L_p = 0$, $L_p = H/6$ and $L_p = H/3$. Black, blue and red colours are utilized to reflect a change in the elastic length scale parameter values from $L_g = 0$ to $L_g = H/3$. From left to right, results correspond to the energetic length scale parameter taken with values $L_e = 0$, $L_e = H/6$ and $L_e = H/3$.

In Fig. 4.12, reaction bending moment per unit width normalized by $H^2\sigma_0$ is plotted against normalized bending curvature, where curves are displayed only for $kH = 0.02$. For $L_g = 0$, the black curves show the results within

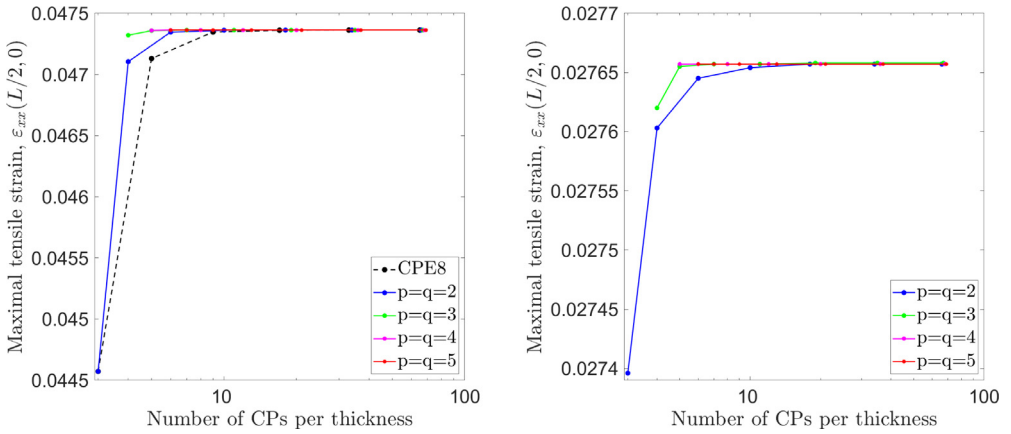


**Fig. 4.10.** Bending of a strip. Convergence of the maximal tensile strain $\varepsilon_{xx}(L/2,0)$ for $L_g = 0$ (left) and $L_g = H/3$ (right). $p$ and $q$ stand for the B-Spline degree within IGA. CPE8 indicates the results using 8-node biquadratic plane strain finite elements. (For interpretation of the references to colour in this figure legend, the reader is referred to the web version of this article.)

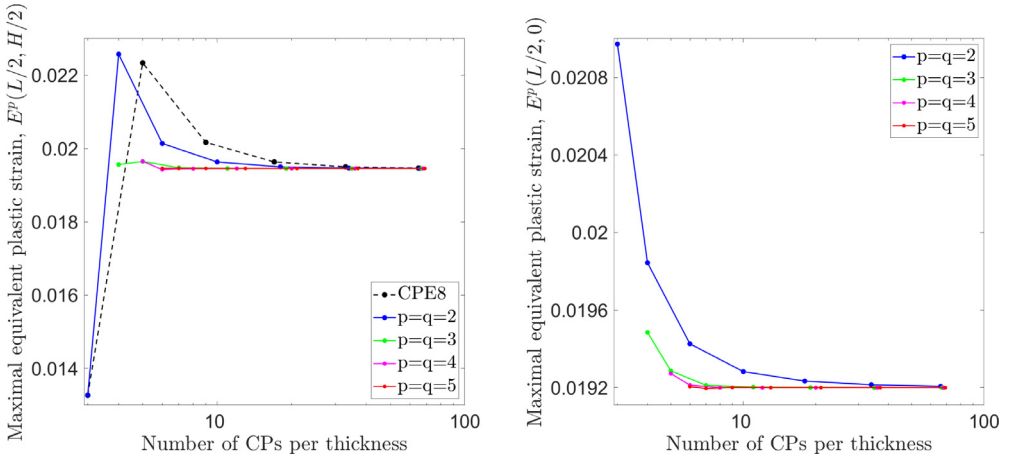


**Fig. 4.11.** Bending of a strip. Convergence of the maximal equivalent plastic strain $E^p(L/2,H/2)$ for $L_g = 0$ (left) and $E^p(L/2,0)$ for $L_g = H/3$ (right). $p$ and $q$ stand for the B-Spline degree within IGA. CPE8 indicates the results using 8-node biquadratic plane strain finite elements. (For interpretation of the references to colour in this figure legend, the reader is referred to the web version of this article.)

SGP model. It can be clearly seen that the dissipative and energetic length scales are responsible for, respectively, dissipative (yield) strengthening and energetic hardening [20]. As in Section 4.1, when the elastic length scale comes into play, the SGEP model demonstrates its capability of capturing materials stiffening phenomenon. This is reflected by the increase in the slope of the elastic part of the curves when the sample size is comparable with the materials elastic length scale. It can also be observed that the elasticity-related length scale parameter, on the one hand, significantly influences the hardening (level of the curves after yielding point) when the energetic length scale parameter is active and of the same magnitude as the elastic one. On the other hand, the effect is minor when the energetic length scale is negligible. Regarding materials (yield) strengthening phenomenon, there is no significant effect from gradient-elastic part of the SGEP model.

Distributions of the plastic tensile strain and equivalent plastic strain fields along the strip thickness at $x = L/2$ are plotted, respectively, in Figs. 4.13 and 4.14. For the plastic tensile strains, it can be observed that the plasticity-related length scales alone (black lines in Fig. 4.13) cause nonlinearity in distribution and lead to decrease in amplitude of the plastic strains. When the energetic length scale increases, the solid, dotted and dashed lines of the same colour tend to overlap, which indicates that the strain profiles are mainly affected by the elastic rather than the dissipative length scale. Regarding the equivalent plastic strain, due to the presence of plastic strain gradients

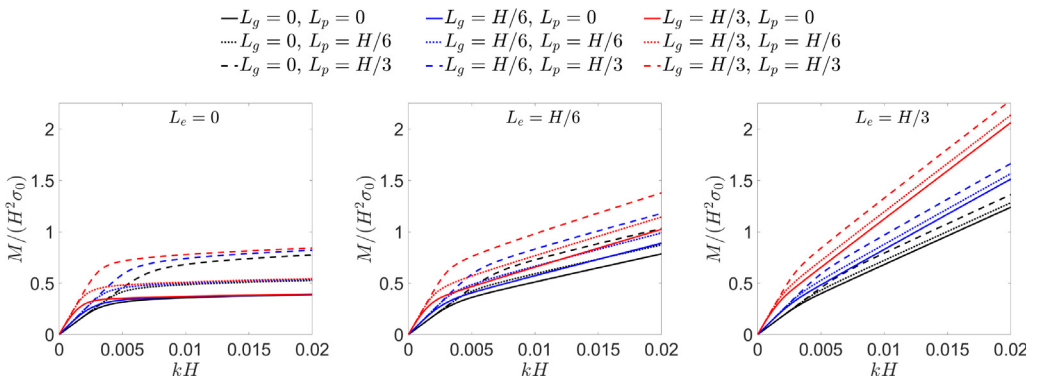


**Fig. 4.12.** Bending of a strip. Normalized bending moment versus normalized bending curvature for $L_e = 0$ (left), $L_e = H/6$ (middle) and $L_e = H/3$ (right). (For interpretation of the references to colour in this figure legend, the reader is referred to the web version of this article.)

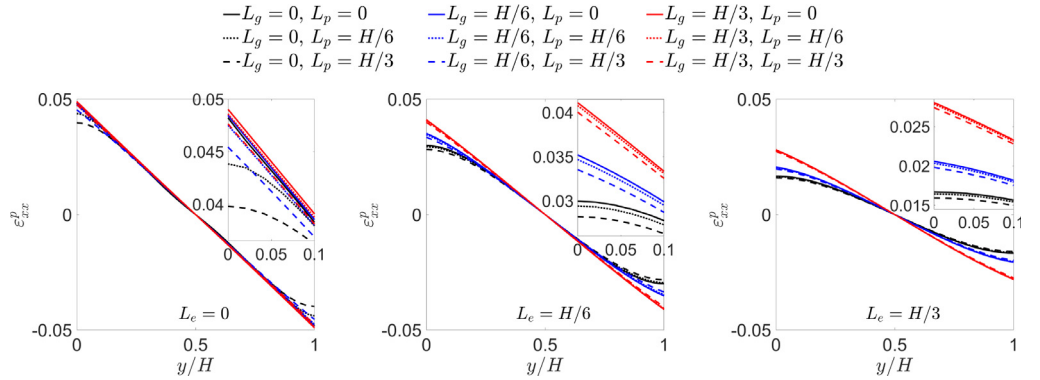


**Fig. 4.13.** Bending of a strip. Distribution of the plastic tensile strain field along the strip thickness at $x = L/2$ for $L_e = 0$ (left), $L_e = H/6$ (middle) and $L_e = H/3$ (right). (For interpretation of the references to colour in this figure legend, the reader is referred to the web version of this article.)

in (2.20), there is a qualitative and quantitative change of the strain profiles. It can be seen that the dissipative length scale gives rise to the strain in the vicinity of the middle line (solid versus dotted and dashed lines in Fig. 4.14). As long as the energetic length scale increases the effect of the dissipative length scale decreases but remains strong. At the same time, the elastic length scale affects the magnitude of strain profiles.

Influence of the viscoplastic exponent $m$ is presented in Fig. 4.8 (right). Results correspond to a classical plasticity model, i.e., all length scale parameters are set to zero. Abaqus built-in rate-independent Johnson–Cook plasticity model (see details in Abaqus Analysis User's Manual [119]) provides a reference curve. It can be seen that the rate-independent material response is retrieved as the viscoplastic exponent tends to zero. For $m = 0.001$, the red dots lie almost exactly on the black curve.

### *4.3. Uniaxial stretching of a plate with a hole*

Let us consider a square thick plate (with side length $L$) weakened by a central circular hole (with radius $a$) under uniaxial stretching. A quarter of the plate section is shown in Fig. 4.15 (left) with a Cartesian coordinate system placed at the hole centre. Plate side length to radius ratio is set to $L/a = 20$.

The plate is modelled using a single (in the $z$-direction) layer of 3D elements (knot spans). The domain is initially split by four knot spans as shown in Fig. 4.15 (left). Then, each knot span is discretized by $32 \times 32 \times 1$ elements forming a mesh of 4096 elements with NURBS of degree 2 providing $C^1$ global continuity. Fig. 4.15 (right) shows the plane view of the mesh around the hole. Within a plane strain problem formulation, $u_z$, $\varepsilon^p_{xz}$ and $\varepsilon^p_{yz}$ are set to

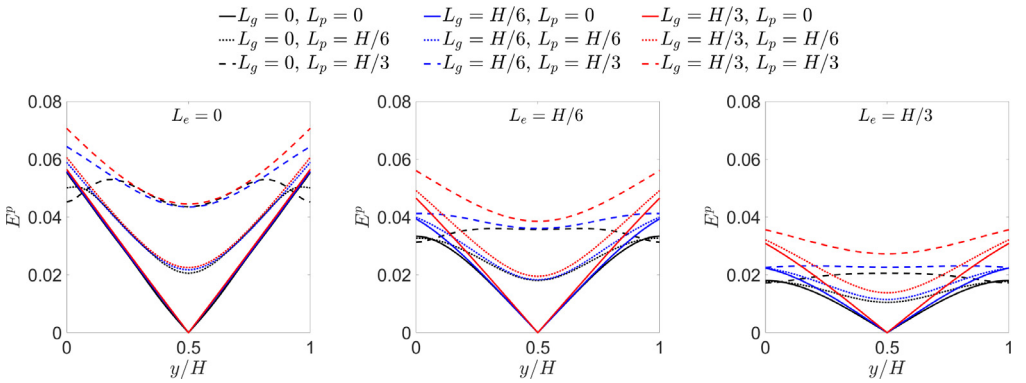


**Fig. 4.14.** Bending of a strip. Distribution of the equivalent plastic strain field along the strip thickness at $x = L/2$ for $L_e = 0$ (left), $L_e = H/6$ (middle) and $L_e = H/3$ (right). (For interpretation of the references to colour in this figure legend, the reader is referred to the web version of this article.)

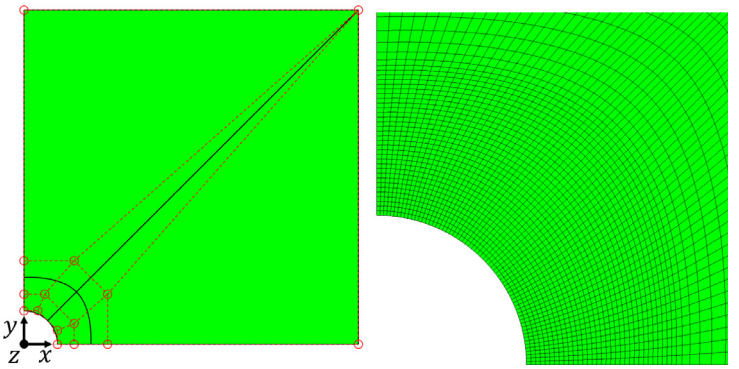


**Fig. 4.15.** Plate with a hole problem. Left: Quarter of the plate section and initial discretization by four knot spans. Right: Plane view of the mesh in the vicinity of the hole. (For interpretation of the references to colour in this figure legend, the reader is referred to the web version of this article.)

zero in the whole domain. For SGP model, the symmetry conditions are then fulfilled by applying $u_x = 0$ and $\varepsilon^p_{xy} = 0$ at the left ($x = 0$) surface and $u_y = 0$ and $\varepsilon^p_{xy} = 0$ at the bottom ($y = 0$) surface. Within SGEP model, the following additional symmetry conditions are prescribed: $\partial u_y/\partial x = 0$ at $x = 0$ and $\partial u_x/\partial y = 0$ at $y = 0$. The plate is stretched by applied displacement $u_y = L/100$ at $y = L/2$ with loading rate $\dot{u}_y/L = 0.01\ \mathrm{s}^{-1}$.

Influence of the length scale parameters on the distribution of the equivalent plastic strain field in the vicinity of the hole is presented in Figs. 4.16–4.18. Distributions of the von Mises Cauchy stress are depicted in Fig. 4.19. Solid, dotted and dashed lines in Figs. 4.18 and 4.19 represent a variation in the dissipative length scale parameter with values set, respectively, to $L_p = 0$, $L_p = a/10$ and $L_p = a/5$. Black, blue and red colours are used to reflect a change in the elastic length scale parameter values from $L_g = 0$ to $L_g = a/2$. From left to right, results correspond to the energetic length scale parameter taken with values $L_e = 0$, $L_e = a/10$ and $L_e = a/5$. In Fig. 4.18 (left), when the energetic length scale is not active, it can be seen that increase in the dissipative length scale leads to significant decrease in the strain magnitude. When the energetic length scale comes into play, it leads to general decrease in the strain magnitude, whereas the elastic and dissipative length scales cause minor variation in the strain profiles.

Regarding stresses, we put our attention to Cauchy stress and consider the stress invariant in the form of von Mises stresses as presented in Fig. 4.19. First, we analyze the interplay between the elastic and dissipative length scales in case when the energetic length scale is not active ($L_e = 0$). It can be seen that when $L_g = 0$ (SGP model), increase in the $L_p$-parameter value from 0 to $a/5$ leads to approximately fourfold increase in the stress magnitude in the vicinity of the hole (from the black solid to black dashed lines). When the $L_g$-parameter is nonzero (SGEP

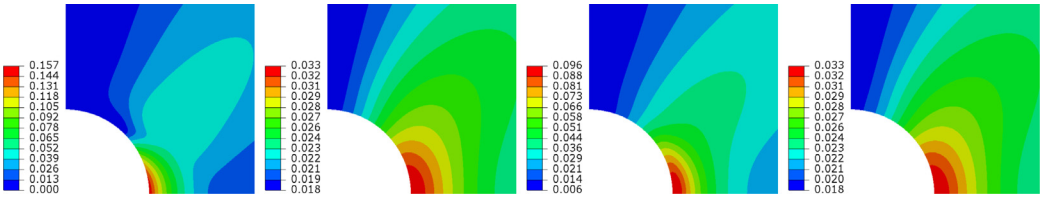

**Fig. 4.16.** Plate with a hole problem. Distribution of the equivalent plastic strain field $E^p$ in the vicinity of the hole within SGP model ($L_g = 0$) for $L_p = 0$ and $L_e = 0$ (1st item), $L_p = 0$ and $L_e = a/5$ (2nd item), $L_p = a/5$ and $L_e = 0$ (3rd item) and $L_p = a/5$ and $L_e = a/5$ (4th item). (For interpretation of the references to colour in this figure legend, the reader is referred to the web version of this article.)

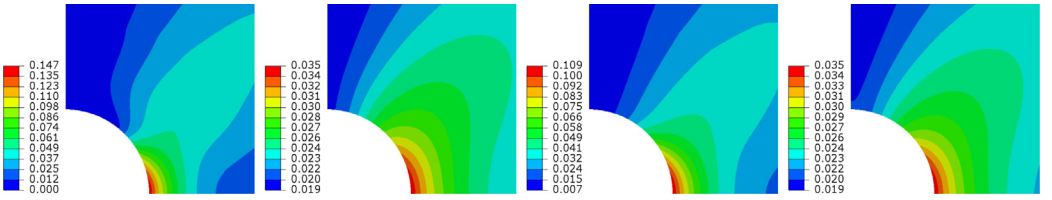

**Fig. 4.17.** Plate with a hole problem. Distribution of the equivalent plastic strain field $E^p$ in the vicinity of the hole within SGEP model ($L_g = a/2$) for $L_p = 0$ and $L_e = 0$ (1st item), $L_p = 0$ and $L_e = a/5$ (2nd item), $L_p = a/5$ and $L_e = 0$ (3rd item) and $L_p = a/5$ and $L_e = a/5$ (4th item). (For interpretation of the references to colour in this figure legend, the reader is referred to the web version of this article.)

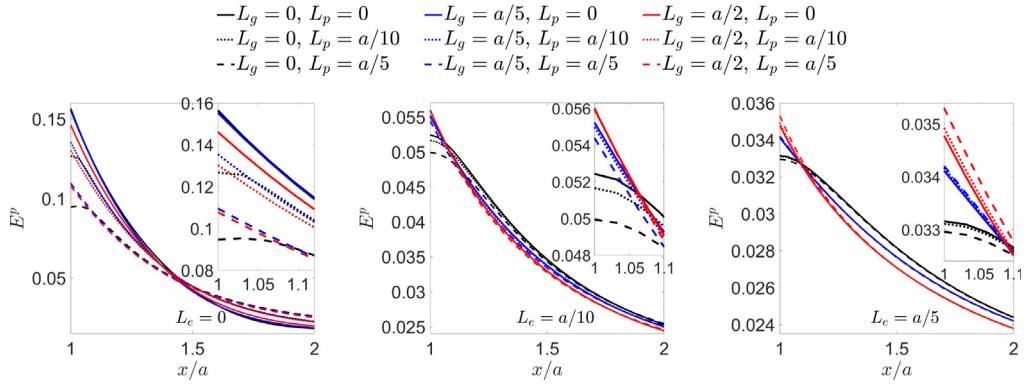


**Fig. 4.18.** Plate with a hole problem. Distribution of the equivalent plastic strain field $E^p$ along line $y = 0$ for $L_e = 0$ (left), $L_e = a/10$ (middle) and $L_e = a/5$ (right). (For interpretation of the references to colour in this figure legend, the reader is referred to the web version of this article.)

model), the higher the $L_g$-parameter value the lower stresses are (from the dashed black to dashed red lines, for instance). Next, we analyze the interplay between the elastic and dissipative length scales in case when the energetic length scale comes into play ($L_e = a/10$ and $L_e = a/5$). It can be seen that the effect of the dissipative length scale is negligible (within each colour the solid, dotted and dashed lines overlap). The influence of the elastic length scale remains strong. For cases when the $L_e$-parameter is getting nonzero, the stress magnitudes are significantly increased as it can be clearly seen for solid lines ($L_p = 0$), for instance. A comprehensive stress and strain analysis is left for future research, however (see [122] for detailed analytical and numerical analyses of the problem in the elastic regime).

For cases when all length scale parameters are set to zero, influence of the viscoplastic exponent $m$ and convergence to a solution obtained within the conventional rate-independent plasticity model is demonstrated in Fig. 4.20 (left). Abaqus built-in rate-independent Johnson–Cook plasticity model (see details in Abaqus Analysis

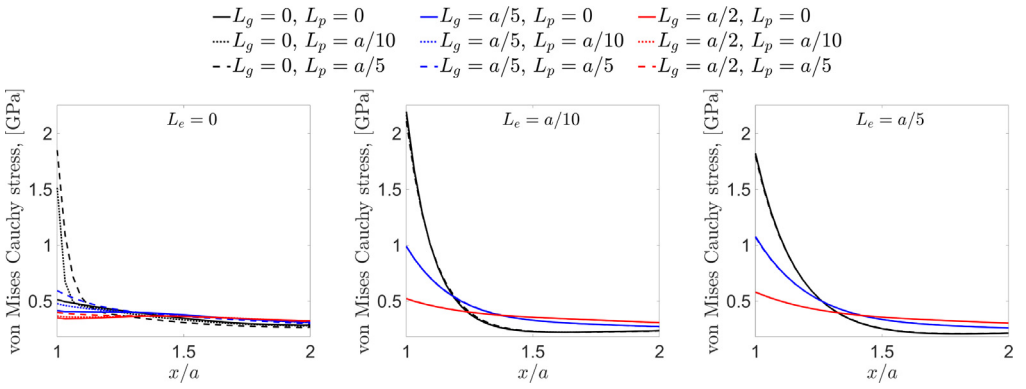


**Fig. 4.19.** Plate with a hole problem. Distribution of the von Mises Cauchy stress field along line $y = 0$ for $L_e = 0$ (left), $L_e = a/10$ (middle) and $L_e = a/5$ (right). (For interpretation of the references to colour in this figure legend, the reader is referred to the web version of this article.)

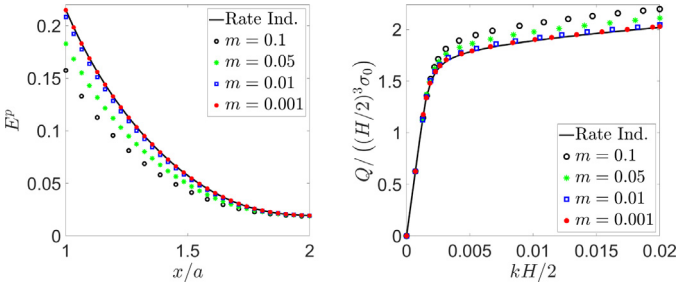


**Fig. 4.20.** Influence of the viscoplastic exponent $m$ on the material response curves for $L_g = L_p = L_e = 0$. Left: Distribution of the equivalent plastic strain field along line $y = 0$ for plate with a hole problem. Right: Normalized reaction torque versus normalized twist for torsion problem. Black solid line represents the solution obtained within conventional rate-independent plasticity model. (For interpretation of the references to colour in this figure legend, the reader is referred to the web version of this article.)

User's Manual [119]) provides a reference curve. It can be seen that the rate-independent material response is retrieved as the viscoplastic exponent tends to zero. For $m = 0.001$, the red dots lie almost exactly on the black curve.

### *4.4. Torsion of a cubic prism*

As a final benchmark we consider a torsion problem of a cubic prism with side length equal to $H$. A Cartesian coordinate system is placed at the cube corner as shown in Fig. 4.24 (left). The bottom surface ($Z = 0$) is pinned, i.e., all displacement components equal to zero, while the top surface ($Z = H$) is restricted in the $Z$-direction. All components of the plastic strain tensor are set to zero at the top and bottom surfaces. The top surface is rotated as a rigid body either by applying the torque or by prescribing the rotation. The rotation axis passes through points $(H/2,\ H/2,\ 0)$ and $(H/2,\ H/2,\ H)$. The rest of the cube faces has zero traction forces. The cube torsion problem is modelled by $N_e \times N_e \times N_e$ three dimensional elements (knot spans) with B-splines of degree $p = q = r$ and $C^{p-1}$ global continuity. For applied torque $Q = 1000$ Nmm, the dissipative and energetic length scale parameter values are set, respectively, to $L_p = H/10$ and $L_e = H/4$.

Figs. 4.21–4.23, within SGP ($L_g = 0$, left) and SGEP ($L_g = H/4$, right) models, show the convergence of, respectively, the maximal displacement, shear strain and equivalent plastic strain for the different polynomial orders. In Fig. 4.21, the converged solution is $u_x(0, 0, H)/H = 0.0692$ (SGP model) and $u_x(0, 0, H)/H = 0.0448$ (SGEP model). In Fig. 4.22, the converged solution is $\varepsilon_{xz}(H, H/2, H/2) = 0.0488$ (SGP model) and $\varepsilon_{xz}(H, H/2, H/2) = 0.0286$ (SGEP model). In Fig. 4.23, the converged solution is $E^p(H, H, H/2) = 0.0198$ (SGP model) and $E^p(H, H, H/2) = 0.0244$ (SGEP model). For polynomial orders $q \geq 3$ the convergence is quite

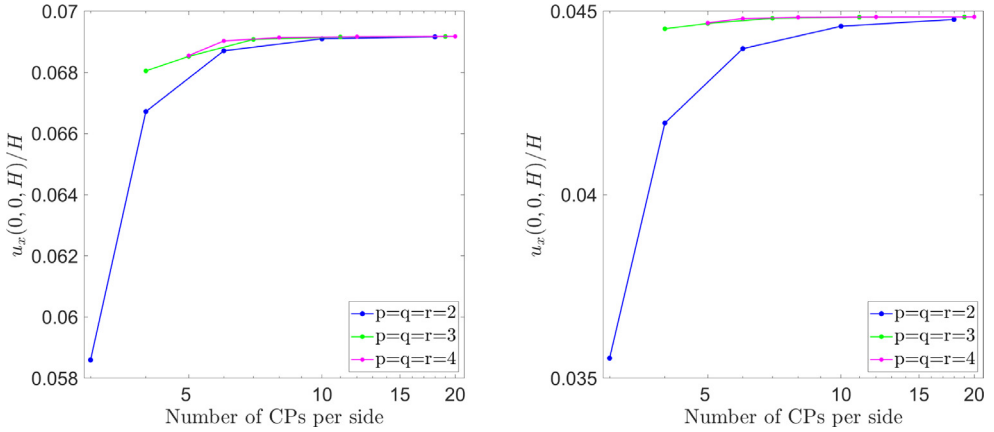


**Fig. 4.21.** Torsion of a constrained cube. Convergence of the maximal displacement, e.g., $u_x(0,0,H)$, normalized by the cube side length for $L_g = 0$ (left) and $L_g = H/4$ (right). (For interpretation of the references to colour in this figure legend, the reader is referred to the web version of this article.)

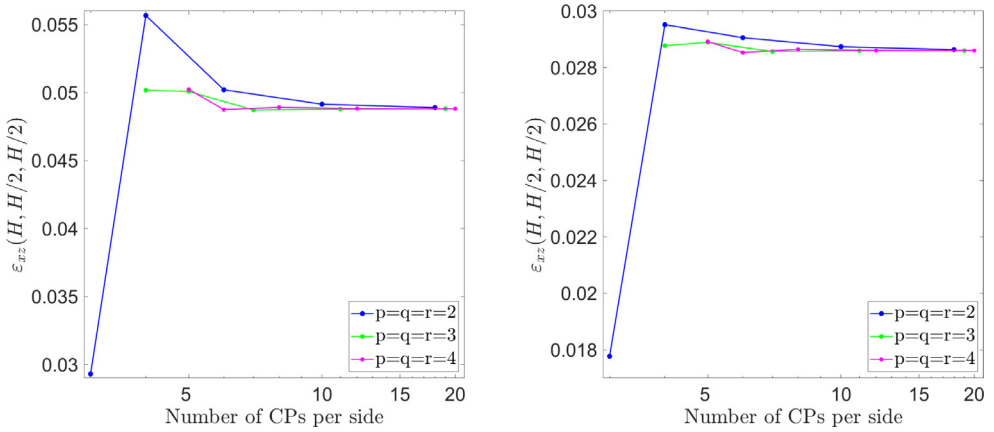


**Fig. 4.22.** Torsion of a constrained cube. Convergence of the maximal total shear strain $\varepsilon_{xz}(H, H/2, H/2)$ for $L_g = 0$ (left) and $L_g = H/4$ (right). (For interpretation of the references to colour in this figure legend, the reader is referred to the web version of this article.)

fast. For quartic shape functions already the second (with respect to displacements) and third (with respect to total shear and equivalent plastic strains) refinement steps yield the converged solution.

Figs. 4.24 and 4.25 show the material response within, respectively, SGP ($L_g = 0$) and SGEP ($L_g = H/4$) models for $L_p = H/10$ and $L_e = H/4$. Distribution of the total shear strain field $\varepsilon_{xz}$ is represented by the 1st item, plastic shear strain field $\varepsilon^p_{xz}$ by the 2nd item and equivalent plastic strain field $E^p$ by the 3rd item. The domain is discretized by $8 \times 8 \times 8$ elements (knot spans) with B-Splines of degree 3 providing $C^2$ global continuity. For visualization purposes, quarter of the elements is hidden.

Next, the brick is twisted by prescribed rotation 0.04 rad (with loading rate 0.04 rad/s) resulting in the normalized twist $kH/2 = 0.02$. Figs. 4.26–4.29 demonstrate material response for different values of the elastic, dissipative and energetic length scale parameters. Solid, dotted and dashed lines represent a variation in the dissipative length scale parameter with values set, respectively, to $L_p = H/100$, $L_p = H/8$ and $L_p = H/4$. Black, blue and red colours are utilized to reflect a change in the elastic length scale parameter values from $L_g = 0$ to $L_g = H/4$. From left to right, results correspond to the energetic length scale parameter taken with values $L_e = H/100$, $L_e = H/16$ and $L_e = H/8$. In Fig. 4.26, reaction torque normalized by $(H/2)^3\sigma_0$ is plotted against normalized twist $kH/2$. For $L_g = 0$, the black curves show the results within SGP model. It can be clearly seen that the dissipative and energetic length scales are responsible for, respectively, dissipative (yield) strengthening and energetic hardening [20]. As in Sections 4.1 and 4.2, when the elastic length scale comes into play, the SGEP model demonstrates its capability of

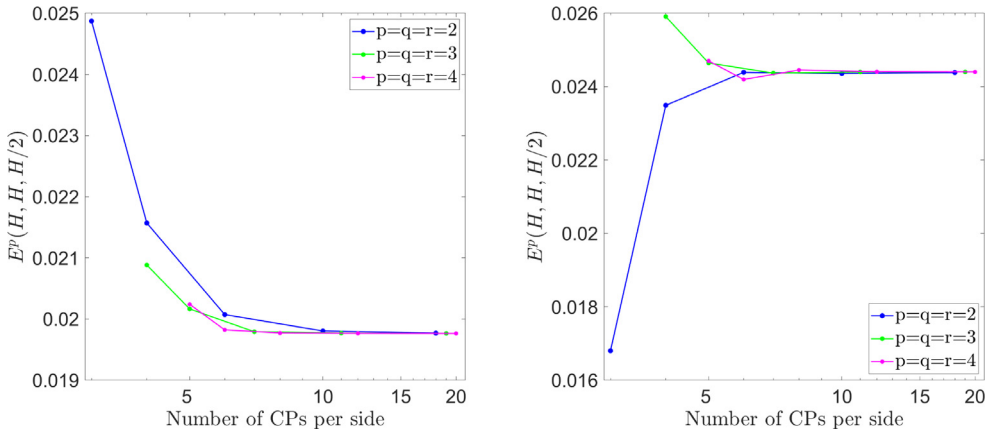


**Fig. 4.23.** Torsion of a constrained cube. Convergence of the equivalent plastic strain $E^p$, e.g., at point $(H,\ H,\ H/2)$, for $L_g = 0$ (left) and $L_g = H/4$ (right). (For interpretation of the references to colour in this figure legend, the reader is referred to the web version of this article.)

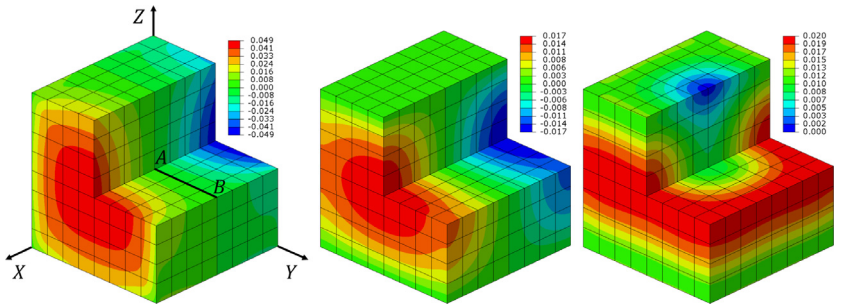


**Fig. 4.24.** Torsion of a constrained cube by applied torque. Distribution of the total shear strain field $\varepsilon_{xz}$ (1st item), plastic shear strain field $\varepsilon^p_{xz}$ (2nd item) and equivalent plastic strain field $E^p$ (3rd item) within SGP ($L_g = 0$) for $L_p = H/10$ and $L_e = H/4$. (For interpretation of the references to colour in this figure legend, the reader is referred to the web version of this article.)

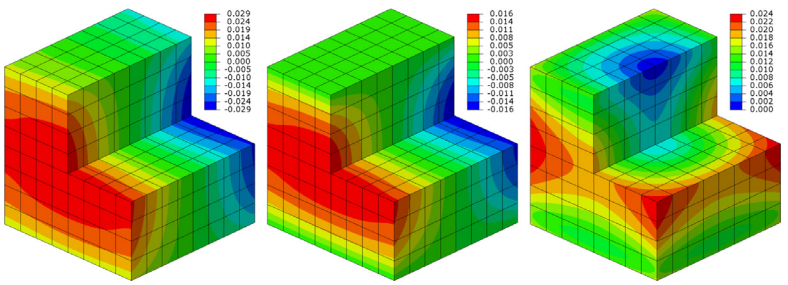

**Fig. 4.25.** Torsion of a constrained cube by applied torque. Distribution of the total shear strain field $\varepsilon_{xz}$ (1st item), plastic shear strain field $\varepsilon^p_{xz}$ (2nd item) and equivalent plastic strain field $E^p$ (3rd item) within SGEP ($L_g = H/4$) for $L_p = H/10$ and $L_e = H/4$. (For interpretation of the references to colour in this figure legend, the reader is referred to the web version of this article.)

capturing materials stiffening phenomenon. This is reflected by the increase in the slope of the elastic part of the curves when the sample size is comparable with the materials elastic length scale. It can also be observed that the elasticity-related length scale parameter, on the one hand, significantly influences the hardening (level of the curves after yielding point) when the energetic length scale parameter is active and of the same magnitude as the elastic one. On the other hand, the effect is minor when the energetic length scale is negligible. Regarding materials (yield) strengthening phenomenon, there is no significant effect from gradient-elastic part of the SGEP model.

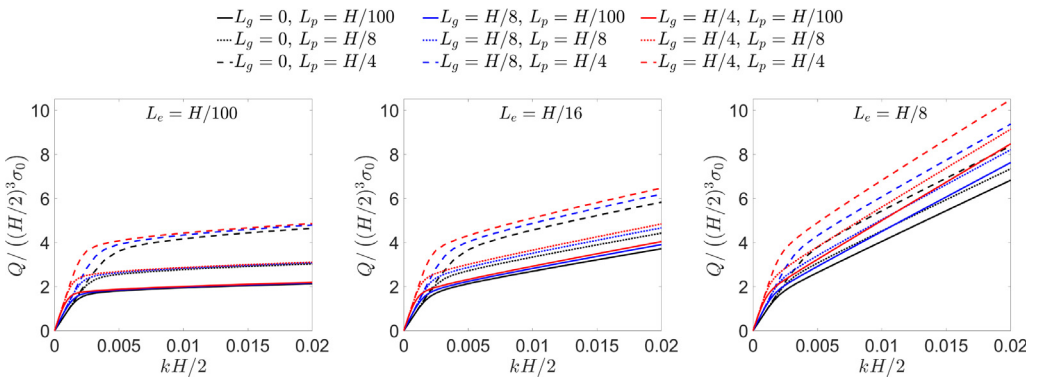


**Fig. 4.26.** Torsion of a constrained cube by prescribed rotation. Normalized reaction torque $Q/\left((H/2)^3\sigma_0\right)$ versus normalized twist $kH/2$ for $L_e = H/100$ (left), $L_e = H/16$ (middle) and $L_e = H/8$ (right). (For interpretation of the references to colour in this figure legend, the reader is referred to the web version of this article.)

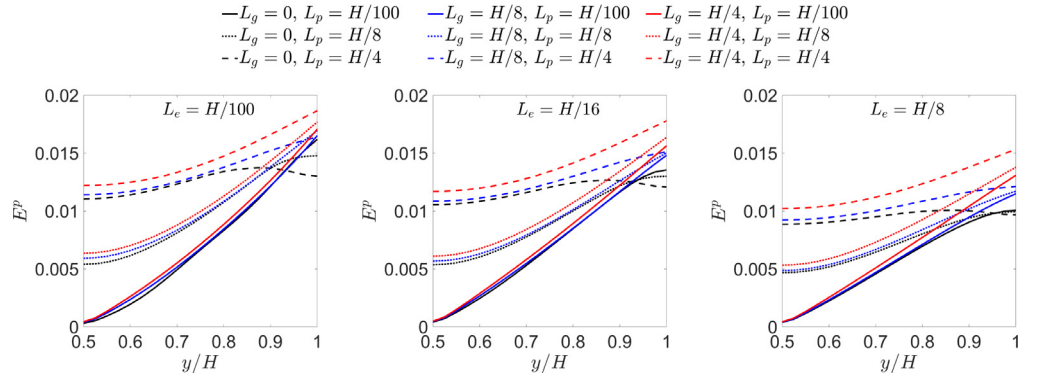


**Fig. 4.27.** Torsion of a constrained cube by prescribed rotation. Distribution of the equivalent plastic strain field $E^p$ along line $X = H/2$, $Z = H/2$, $H/2 \le Y \le H$ (path $AB$ shown in Fig. 4.24, 1st item) for $L_e = H/100$ (left), $L_e = H/16$ (middle) and $L_e = H/8$ (right). (For interpretation of the references to colour in this figure legend, the reader is referred to the web version of this article.)

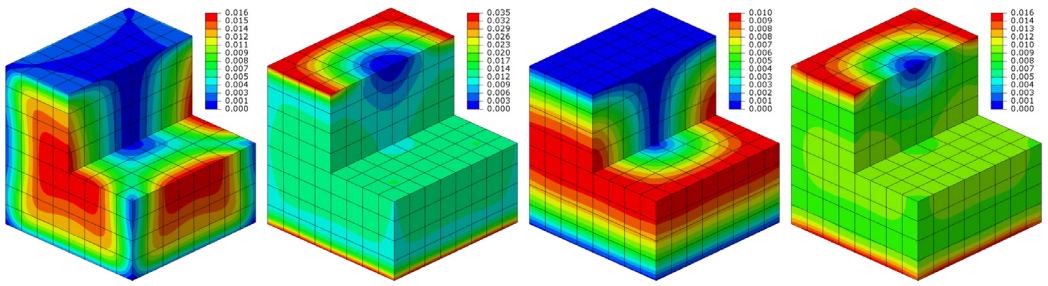

**Fig. 4.28.** Torsion of a constrained cube by prescribed rotation. Distribution of the equivalent plastic strain field $E^p$ within SGP ($L_g = 0$) for $L_p = H/100$ and $L_e = H/100$ (1st item), $L_p = H/4$ and $L_e = H/100$ (2nd item), $L_p = H/100$ and $L_e = H/8$ (3rd item) and $L_p = H/4$ and $L_e = H/8$ (4th item). (For interpretation of the references to colour in this figure legend, the reader is referred to the web version of this article.)

Figs. 4.27, 4.28 and 4.29 demonstrate the distribution of the equivalent plastic strain fields. In Fig. 4.27, the equivalent plastic strain is plotted along path $AB$ (shown in Fig. 4.24 (left)). It can be seen that the energetic and elastic length scales affect the magnitude of strain profiles. Due to the presence of plastic strain gradients in (2.20), the dissipative length scale gives rise to the strain in the vicinity of point $A$ (solid versus dotted and dashed lines in Fig. 4.27).

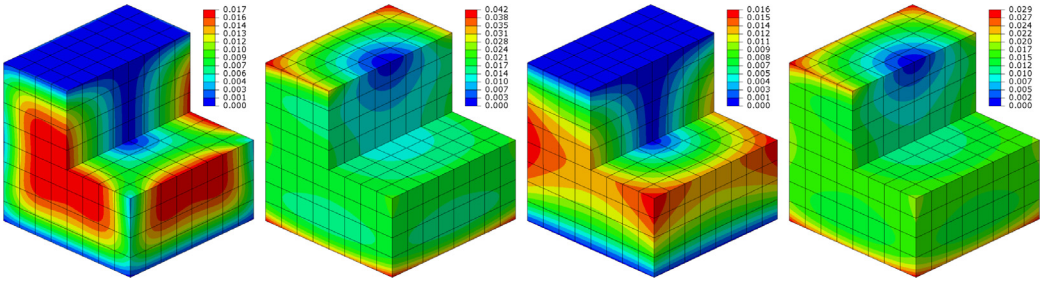

**Fig. 4.29.** Torsion of a constrained cube by prescribed rotation. Distribution of the equivalent plastic strain field $E^p$ within SGEP ($L_g = H/4$) for $L_p = H/100$ and $L_e = H/100$ (1st item), $L_p = H/4$ and $L_e = H/100$ (2nd item), $L_p = H/100$ and $L_e = H/8$ (3rd item) and $L_p = H/4$ and $L_e = H/8$ (4th item). (For interpretation of the references to colour in this figure legend, the reader is referred to the web version of this article.)

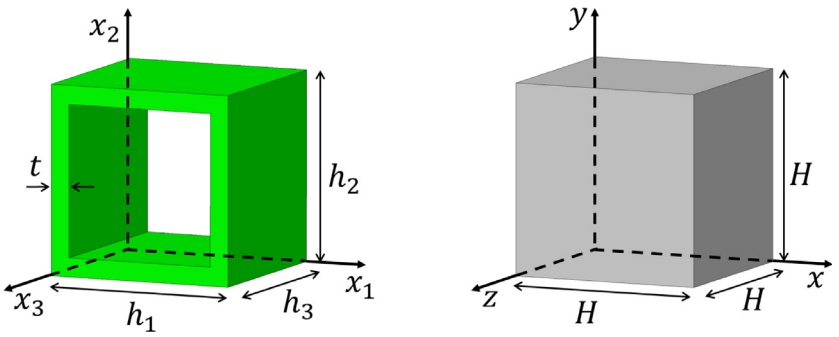


**Fig. 5.1.** Left: Unit cell of the square cellular structure with dimensions. Right: Continuum representation of the microstructural samples.

Influence of the viscoplastic exponent $m$ is depicted in Fig. 4.20 (right), where results correspond to a classical plasticity model, i.e., all length scale parameters are set to zero and all plastic strain components are released on the top and bottom surfaces. The reference strain rate is set to $\dot{\varepsilon}_0 = 0.004\ \mathrm{s}^{-1}$ for that case. Abaqus built-in rate-independent Johnson–Cook plasticity model (see details in Abaqus Analysis User's Manual [119]) provides a reference curve. It can be seen that the rate-independent material response is retrieved as the viscoplastic exponent tends to zero. For $m = 0.001$, the red dots lie almost exactly on the black curve.

## 5. Application to cellular structures

In this section, we consider a torsion problem of structures possessing cellular microarchitecture. The unit cell is shown in Fig. 5.1 (left) with $h_1 = h_2 = h_3 = h = 10$ mm and $t = 1$ mm resulting in relative density $\bar{\rho} = 36\%$. The base material of the microstructure follows the classical isotropic elasto-plastic model with linear hardening, i.e., exponent $N = 1$ in Johnson–Cook plasticity model, with the material parameter values listed in Table 1. Regarding the effect of the unit cell thickness, $t$, on the effective material properties, we refer to [29]. In particular, considering the bending of trusses made of the triangular lattice, it has been shown that as long as the relative density decreases and approaches zero the effective Young's modulus follows the same pattern. The effective elastic length scale parameter demonstrates opposite behaviour, i.e., it takes zero value when the relative density is 100% and approaches some nonzero limit value as the relative density tends to zero.

Four samples are virtually tested via computer simulations. The samples have one, two, three and sixteen unit cells in the $x$-, $y$- and $z$-directions resulting, respectively, in the following sample sizes: $H = 10$ mm, $H = 20$ mm, $H = 30$ mm and $H = 160$ mm (see Fig. 5.2). Surfaces with $z = 0$ are pinned, i.e., $u_x = u_y = u_z = 0$. The opposite surfaces with $z = H$ have restricted normal displacements ($u_z = 0$) and are rotated by angle 0.02 rad as a rigid body around the axis passing through points ($H/2$, $H/2$, 0) and ($H/2$, $H/2$, $H$). The samples are discretized by C3D8 (linear fully integrated brick) finite elements with the element side size $t/2$ resulting in two elements per wall thickness of the unit cell. For the sample composed of one unit cell, the convergence analysis has shown

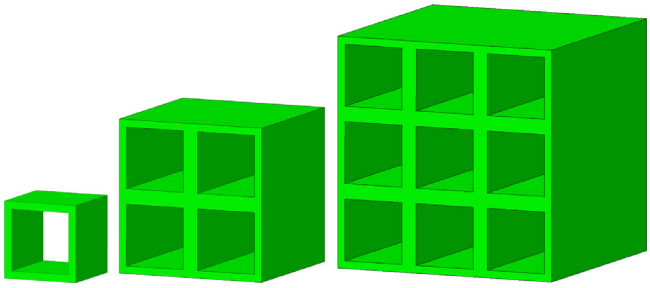

**Fig. 5.2.** Samples with one, two and three unit cells in the $x$-, $y$- and $z$-directions.

**Table 1**
Parameter values for base and effective continuum material models.

| Material | $E$, [GPa] | $\nu$ | $\sigma_0$, [MPa] | $K$, [MPa] | $N$ | $L_g/h$ | $L_p/h$ | $L_e/h$ |
|---|---|---|---|---|---|---|---|---|
| Base | 200 | 0.3 | 200 | 1000 | 1 | – | – | – |
| Effective | 43.42 | 0.3 | 38 | 30 | 0.25 | 0.32 | 0.33 | 0 |

that with the chosen mesh the relative error in reaction torque is less than 0.05% with respect to the mesh of two and less than 0.25% with respect to the mesh of eight C3D20 (quadratic fully integrated brick) finite elements per wall thickness of the unit cell. This deviation is considered to be acceptable when finding compromise between the accuracy and computational cost. Torsional response of the samples, namely normalized reaction torque $Q/(H/2)^3$ versus normalized twist $kH/2$, is presented in Fig. 5.3 as dots.

The size-dependent torsional behaviour is modelled in the framework of strain gradient elasto-plasticity theory by representing the structures with cellular microarchitecture as homogeneous effective continuum (Fig. 5.1 (right)). Torsional response of sample with $H = 160$ mm (black dots in Fig. 5.3) is considered to be sufficiently close to size-independent response of the corresponding classical effective continuum and, hence, is used for calibrating the set of classical material constants. For selected Poisson's ratio (set to $\nu = 0.3$), Young's modulus is defined by fitting the linear elastic part of the curve. Three parameters of the Johnson–Cook plasticity model are defined by fitting the plastic part of the curve.

Next, the elastic length scale parameter is determined by capturing the size-dependent elastic response, i.e., slope of the linear elastic part of the dotted curves. The dissipative length scale parameter, affecting the material yielding, is selected to fit the response of sample with $H = 30$ mm. It should be noted that the considered cellular structures do not demonstrate the energetic hardening phenomenon (in torsion), which is supported by the SGEP continuum model. Hence, the energetic length scale, controlling the slope of the plastic part of stress–strain curves, is omitted in the modelling. The calibrated material parameters of the SGEP model are collected in Table 1 in the bottom row. The reference strain rate and viscoplastic exponent are set, respectively, to $\dot{\varepsilon}_0 = 0.01$ s$^{-1}$ and $m = 0.001$ in order to minimize the rate-dependent effect.

In Fig. 5.3, the simulation results within the SGEP model are plotted as solid lines and within the SGP model as dashed lines. Black, blue, green, and red colours are utilized, respectively, for cases when $H = 160$ mm, $H = 30$ mm, $H = 20$ mm, and $H = 10$ mm. It can be seen that when the elastic length scale is active, the continuum model very accurately captures the material stiffening phenomenon. Regarding the strengthening and hardening phenomena, both continuum models underestimate the response of sample with $H = 10$ mm and overestimate the response of sample with $H = 20$ mm. However, the red solid curve (SGEP model) lies much closer to the red dots (sample with $H = 10$ mm). The model improvements and corresponding research prospects are addressed in detail in Section 6.

A comment regarding the effective material properties utilized in the SGEP and SGP models should be given. As it can be seen in Fig. 5.3, the black solid and dashed curves overlap and fit the black dots. This indicates that both the SGEP and SGP models share the same effective classical material properties, e.g, Young's modulus. The fact that the blue solid and dashed curves almost identically represent the torsion response (blue dots after material yielding point) of sample with $H = 30$ mm (used for calibration of the dissipative length scale parameter) indicates

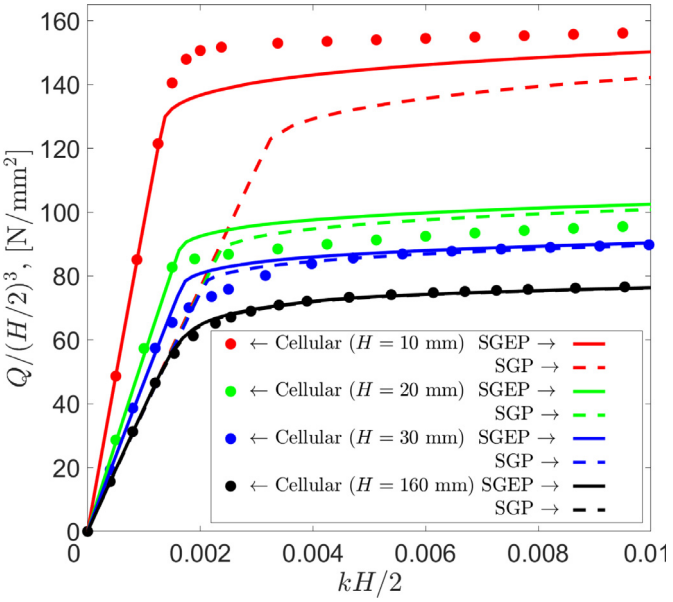


**Fig. 5.3.** Normalized reaction torque $Q/(H/2)^3$ versus normalized twist $kH/2$. Dotted curves correspond to torsional response of cellular structures. Solid and dashed lines represent the results within SGEP and SGP effective continuum models. (For interpretation of the references to colour in this figure legend, the reader is referred to the web version of this article.)

that both the SGEP and SGP models share the same effective plasticity-related higher-order material properties, namely the $L_p$-parameter.

## 6. Concluding remarks and prospects

In the current work, a strain gradient elasto-plasticity continuum model has been considered as an extension of SGP theory proposed by Gudmundson in [14]. The present SGEP model takes into account the gradient of elastic strains in the expressions of the internal virtual work and free energy. The governing equations, boundary conditions and variational formulations have been derived. A three-parameter variant has been considered, namely, SGEP model with one elasticity-related and two plasticity-related (energetic and dissipative) length scale parameters. The conforming Galerkin method has been formulated and implemented by utilizing an isogeometric $C^{p-1}$-continuous approach with NURBS basis functions of degree $p \geq 2$. Following [63,64], a viscoplastic constitutive framework based on the backward (implicit) Euler time integration scheme has been adopted. The implementation has been verified by comparing the results with the SGP model implementation based on biquadratic $C^0$-continuous plane strain finite elements [64], and by demonstrating a transition to the rate-independent case of the conventional plasticity model.

A set of benchmark problems has been considered for confirming the convergence properties of the method. By accomplishing a parametric study and analyzing the material response curves in Figs. 4.4, 4.12 and 4.26, respectively, for the shear, bending and torsion benchmark problems, we report that the elasticity-related length scale parameter: (i) controls the slope of the elastic part; (ii) significantly influences the hardening (the level and the slope of the plastic part) when the energetic length scale parameter is active and of the same magnitude as the elastic one; (iii) slightly affects the hardening when the energetic length scale is negligible. It also influences the amplitude and overall distribution of the strain fields as shown in Figs. 4.5–4.7, 4.13, 4.14, 4.24, 4.25, 4.27, 4.28, and 4.29. In a stretching problem of Section 4.3, the (von Mises) Cauchy stress distribution in the vicinity of the hole (Fig. 4.19) has shown to be significantly affected by presence of the elasticity-related length scale. This motivates for a comprehensive stress and strain field analyses as a future research topic (see [122], where main characters of the gradient-elastic stress fields were analyzed by analytical and numerical means).

An illustrative example has been considered to examine the applicability of the SGEP model in capturing the size-dependent torsion response of cellular structures. It has been demonstrated that: (i) there are two distinct purely

elastic and elastic–plastic size effects, (ii) the elastic size effect is captured quantitatively by the SGEP model, while (iii) the plasticity-related size effect is modelled only qualitatively. The latter is believed to be caused by certain limitations of the effective continuum model. In particular, the continuum model covers isotropic materials only, while cellular structures demonstrate, in general, strong anisotropic behaviour (see [32]). Also, the utilized SGEP model falls to the category of the plastically irrotational theories. These open two prospective research directions. The first is an extension of the present isotropic SGEP model towards anisotropic case addressing a full set of symmetry classes defined for gradient elasticity in [123] (see also [124,125] where cellular solids are modelled by anisotropic variant of the conventional plasticity). The second one covers distortion gradient elasto-plasticity, i.e., elastically and plastically rotational theories. The corresponding isogeometric numerical implementations naturally follow alongside.

Regarding the calibration of a set of higher-order elasticity- and plasticity-related material parameters, we highlight two following strategies. Computational homogenization techniques (see [126–133], for instance) are considered to be the first approach, where the constitutive moduli are determined in a phenomenological manner. Variational asymptotic homogenization [134–140] is seen to be another technique, where the constitutive parameters of the homogeneous effective continuum are defined in terms of internal characteristics of the underlying microstructure.

As a relevant research topic, we also consider a development of dimensionally reduced SGEP models for beam, plate and shell structural elements as extensions of the gradient-elastic Bernoulli–Euler [91] and locking-free Timoshenko [92] beam models, Kirchhoff plate [95] and Kirchhoff–Love shell [97] models (cf. [141] for conventional elasto-plastic IGA shell model formulation) including thermal effects [31,32] and damage [34,142]. The results of the present work can also serve as a basis for the development of elasto-plastic variant of the Mindlin's second strain gradient elasticity theory, originally proposed in [101] (cf. [143] where only plastic strain gradients are considered). As it is shown in [30,144] with respect to the gradient-elastic coupling terms, the coupling terms and related moduli with respect to plastic strains and second gradient of plastic strains are expected to be of particular interest. For both the dimensionally reduced SGEP models and second strain gradient elasto-plasticity continuum models, $H^3$-conforming Galerkin methods require $C^2$-continuous isogeometric implementations as accompanying numerical realization steps (possibly including some adaptive refinement techniques [145]).

## Declaration of competing interest

The authors declare that they have no known competing financial interests or personal relationships that could have appeared to influence the work reported in this paper.

## Acknowledgements

The authors would like to acknowledge the financial support of Business Finland in the form of a research project ISA VTT Dnro 7980/31/2018. The authors are grateful to Dr. Viacheslav Balobanov from VTT Technical Research Centre of Finland, Dr. Aleksandr Morozov from Technical University of Berlin, and MSc Kseniia Khakalo from Top Data Science Oy for fruitful discussions and useful comments.

## Appendix A. Matrix operators and derivation details

Matrices of basis functions used in the displacement and plastic strain field interpolations in (3.9) are, respectively, defined as

$$\underline{\underline{N}}^{u} = \begin{bmatrix} \underline{\underline{N}}^{u(1)} & \cdots & \underline{\underline{N}}^{u(n)} \end{bmatrix}, \quad \underline{\underline{N}} = \begin{bmatrix} \underline{\underline{N}}^{(1)} & \cdots & \underline{\underline{N}}^{(n)} \end{bmatrix}, \tag{A.1}$$

where for the $i$th control point the submatrices take the form

$$\underline{\underline{N}}^{u(i)} = N^{(i)} \begin{bmatrix} 1 & 0 & 0 \\ 0 & 1 & 0 \\ 0 & 0 & 1 \end{bmatrix}, \quad \underline{\underline{N}}^{(i)} = N^{(i)} \begin{bmatrix} 1 & 0 & 0 & 0 & 0 & 0 \\ 0 & 1 & 0 & 0 & 0 & 0 \\ 0 & 0 & 1 & 0 & 0 & 0 \\ 0 & 0 & 0 & 1 & 0 & 0 \\ 0 & 0 & 0 & 0 & 1 & 0 \\ 0 & 0 & 0 & 0 & 0 & 1 \end{bmatrix} \tag{A.2}$$

with $i = 1, \ldots, n$ and $n$ standing for the total number of control points.

Matrices of the basis function derivatives used in the total strain, total strain gradient and plastic strain gradient field interpolations in (3.12) are, respectively, specified as

$$\underline{\underline{B}} = \left[\underline{\underline{B}}^{(1)} \cdots \underline{\underline{B}}^{(n)}\right], \quad \underline{\underline{L}} = \left[\underline{\underline{L}}^{(1)} \cdots \underline{\underline{L}}^{(n)}\right], \quad \underline{\underline{M}} = \left[\underline{\underline{M}}^{(1)} \cdots \underline{\underline{M}}^{(n)}\right], \tag{A.3}$$

with

$$\underline{\underline{B}}^{(i)} = \begin{bmatrix} \frac{\partial N^{(i)}}{\partial x} & 0 & 0 \\ 0 & \frac{\partial N^{(i)}}{\partial y} & 0 \\ 0 & 0 & \frac{\partial N^{(i)}}{\partial z} \\ 0 & \frac{\partial N^{(i)}}{\partial z} & \frac{\partial N^{(i)}}{\partial y} \\ \frac{\partial N^{(i)}}{\partial z} & 0 & \frac{\partial N^{(i)}}{\partial x} \\ \frac{\partial N^{(i)}}{\partial y} & \frac{\partial N^{(i)}}{\partial x} & 0 \end{bmatrix},$$

$$\underline{\underline{L}}^{(i)} = \begin{bmatrix} \frac{\partial^2 N^{(i)}}{\partial x^2} & 0 & 0 \\ \frac{\partial^2 N^{(i)}}{\partial x \partial y} & 0 & 0 \\ \frac{\partial^2 N^{(i)}}{\partial x \partial z} & 0 & 0 \\ 0 & \frac{\partial^2 N^{(i)}}{\partial x \partial y} & 0 \\ 0 & \frac{\partial^2 N^{(i)}}{\partial y^2} & 0 \\ 0 & \frac{\partial^2 N^{(i)}}{\partial y \partial z} & 0 \\ 0 & 0 & \frac{\partial^2 N^{(i)}}{\partial x \partial z} \\ 0 & 0 & \frac{\partial^2 N^{(i)}}{\partial y \partial z} \\ 0 & 0 & \frac{\partial^2 N^{(i)}}{\partial z^2} \\ 0 & \frac{\partial^2 N^{(i)}}{\partial x \partial z} & \frac{\partial^2 N^{(i)}}{\partial x \partial y} \\ 0 & \frac{\partial^2 N^{(i)}}{\partial y \partial z} & \frac{\partial^2 N^{(i)}}{\partial y^2} \\ 0 & \frac{\partial^2 N^{(i)}}{\partial z^2} & \frac{\partial^2 N^{(i)}}{\partial y \partial z} \\ \frac{\partial^2 N^{(i)}}{\partial x \partial z} & 0 & \frac{\partial^2 N^{(i)}}{\partial x^2} \\ \frac{\partial^2 N^{(i)}}{\partial y \partial z} & 0 & \frac{\partial^2 N^{(i)}}{\partial x \partial y} \\ \frac{\partial^2 N^{(i)}}{\partial z^2} & 0 & \frac{\partial^2 N^{(i)}}{\partial x \partial z} \\ \frac{\partial^2 N^{(i)}}{\partial x \partial y} & \frac{\partial^2 N^{(i)}}{\partial x^2} & 0 \\ \frac{\partial^2 N^{(i)}}{\partial y^2} & \frac{\partial^2 N^{(i)}}{\partial x \partial y} & 0 \\ \frac{\partial^2 N^{(i)}}{\partial y \partial z} & \frac{\partial^2 N^{(i)}}{\partial x \partial z} & 0 \end{bmatrix}, \quad \underline{\underline{M}}^{(i)} = \begin{bmatrix} \frac{\partial N^{(i)}}{\partial x} & 0 & 0 & 0 & 0 & 0 \\ \frac{\partial N^{(i)}}{\partial y} & 0 & 0 & 0 & 0 & 0 \\ \frac{\partial N^{(i)}}{\partial z} & 0 & 0 & 0 & 0 & 0 \\ 0 & \frac{\partial N^{(i)}}{\partial x} & 0 & 0 & 0 & 0 \\ 0 & \frac{\partial N^{(i)}}{\partial y} & 0 & 0 & 0 & 0 \\ 0 & \frac{\partial N^{(i)}}{\partial z} & 0 & 0 & 0 & 0 \\ 0 & 0 & \frac{\partial N^{(i)}}{\partial x} & 0 & 0 & 0 \\ 0 & 0 & \frac{\partial N^{(i)}}{\partial y} & 0 & 0 & 0 \\ 0 & 0 & \frac{\partial N^{(i)}}{\partial z} & 0 & 0 & 0 \\ 0 & 0 & 0 & \frac{\partial N^{(i)}}{\partial x} & 0 & 0 \\ 0 & 0 & 0 & \frac{\partial N^{(i)}}{\partial y} & 0 & 0 \\ 0 & 0 & 0 & \frac{\partial N^{(i)}}{\partial z} & 0 & 0 \\ 0 & 0 & 0 & 0 & \frac{\partial N^{(i)}}{\partial x} & 0 \\ 0 & 0 & 0 & 0 & \frac{\partial N^{(i)}}{\partial y} & 0 \\ 0 & 0 & 0 & 0 & \frac{\partial N^{(i)}}{\partial z} & 0 \\ 0 & 0 & 0 & 0 & 0 & \frac{\partial N^{(i)}}{\partial x} \\ 0 & 0 & 0 & 0 & 0 & \frac{\partial N^{(i)}}{\partial y} \\ 0 & 0 & 0 & 0 & 0 & \frac{\partial N^{(i)}}{\partial z} \end{bmatrix}.$$

The matrices of elastic constants of the isotropic material are written as

$$\underline{\underline{C}} = \begin{bmatrix} 2\mu + \lambda & \lambda & \lambda & 0 & 0 & 0 \\ \lambda & 2\mu + \lambda & \lambda & 0 & 0 & 0 \\ \lambda & \lambda & 2\mu + \lambda & 0 & 0 & 0 \\ 0 & 0 & 0 & \mu & 0 & 0 \\ 0 & 0 & 0 & 0 & \mu & 0 \\ 0 & 0 & 0 & 0 & 0 & \mu \end{bmatrix}, \tag{A.4}$$

$$\underline{\underline{C}}' = \begin{bmatrix} 2\mu & 0 & 0 & 0 & 0 & 0 \\ 0 & 2\mu & 0 & 0 & 0 & 0 \\ 0 & 0 & 2\mu & 0 & 0 & 0 \\ 0 & 0 & 0 & \mu & 0 & 0 \\ 0 & 0 & 0 & 0 & \mu & 0 \\ 0 & 0 & 0 & 0 & 0 & \mu \end{bmatrix}, \tag{A.5}$$

$$\underline{\underline{A}} = L_g^2 \begin{bmatrix} (2\mu+\lambda)\underline{\underline{I}} & \lambda\underline{\underline{I}} & \lambda\underline{\underline{I}} & \underline{\underline{O}} & \underline{\underline{O}} & \underline{\underline{O}} \\ \lambda\underline{\underline{I}} & (2\mu+\lambda)\underline{\underline{I}} & \lambda\underline{\underline{I}} & \underline{\underline{O}} & \underline{\underline{O}} & \underline{\underline{O}} \\ \lambda\underline{\underline{I}} & \lambda\underline{\underline{I}} & (2\mu+\lambda)\underline{\underline{I}} & \underline{\underline{O}} & \underline{\underline{O}} & \underline{\underline{O}} \\ \underline{\underline{O}} & \underline{\underline{O}} & \underline{\underline{O}} & \mu\underline{\underline{I}} & \underline{\underline{O}} & \underline{\underline{O}} \\ \underline{\underline{O}} & \underline{\underline{O}} & \underline{\underline{O}} & \underline{\underline{O}} & \mu\underline{\underline{I}} & \underline{\underline{O}} \\ \underline{\underline{O}} & \underline{\underline{O}} & \underline{\underline{O}} & \underline{\underline{O}} & \underline{\underline{O}} & \mu\underline{\underline{I}} \end{bmatrix}, \tag{A.6}$$

$$\underline{\underline{A}}' = L_g^2 \begin{bmatrix} 2\mu\underline{\underline{I}} & \underline{\underline{O}} & \underline{\underline{O}} & \underline{\underline{O}} & \underline{\underline{O}} & \underline{\underline{O}} \\ \underline{\underline{O}} & 2\mu\underline{\underline{I}} & \underline{\underline{O}} & \underline{\underline{O}} & \underline{\underline{O}} & \underline{\underline{O}} \\ \underline{\underline{O}} & \underline{\underline{O}} & 2\mu\underline{\underline{I}} & \underline{\underline{O}} & \underline{\underline{O}} & \underline{\underline{O}} \\ \underline{\underline{O}} & \underline{\underline{O}} & \underline{\underline{O}} & \mu\underline{\underline{I}} & \underline{\underline{O}} & \underline{\underline{O}} \\ \underline{\underline{O}} & \underline{\underline{O}} & \underline{\underline{O}} & \underline{\underline{O}} & \mu\underline{\underline{I}} & \underline{\underline{O}} \\ \underline{\underline{O}} & \underline{\underline{O}} & \underline{\underline{O}} & \underline{\underline{O}} & \underline{\underline{O}} & \mu\underline{\underline{I}} \end{bmatrix}, \tag{A.7}$$

where

$$\underline{\underline{I}} = \begin{bmatrix} 1 & 0 & 0 \\ 0 & 1 & 0 \\ 0 & 0 & 1 \end{bmatrix}, \quad \underline{\underline{O}} = \begin{bmatrix} 0 & 0 & 0 \\ 0 & 0 & 0 \\ 0 & 0 & 0 \end{bmatrix}. \tag{A.8}$$

Derivative quantities of the integrands of stiffness submatrix (3.19) are explicitly expressed in the following form (cf. [146])

$$\begin{aligned} \frac{\partial \underline{q}^D}{\partial \Delta \underline{\varepsilon}^p} &= \frac{2}{3}\left(\frac{\partial \Sigma}{\partial \Delta E^p}\frac{1}{\Delta E^p} - \frac{\Sigma}{(\Delta E^p)^2}\right)\underline{\underline{H}}_{\varepsilon}\Delta\underline{\varepsilon}^p\left(\frac{\partial \Delta E^p}{\partial \Delta \underline{\varepsilon}^p}\right)^T + \frac{2}{3}\frac{\Sigma}{\Delta E^p}\underline{\underline{H}}_{\varepsilon}, \\ \frac{\partial \underline{q}^D}{\partial \Delta \underline{\nabla\varepsilon}^p} &= \frac{2}{3}\left(\frac{\partial \Sigma}{\partial \Delta E^p}\frac{1}{\Delta E^p} - \frac{\Sigma}{(\Delta E^p)^2}\right)\underline{\underline{H}}_{\varepsilon}\Delta\underline{\varepsilon}^p\left(\frac{\partial \Delta E^p}{\partial \Delta \underline{\nabla\varepsilon}^p}\right)^T, \\ \frac{\partial \underline{m}^D}{\partial \Delta \underline{\nabla\varepsilon}^p} &= L_p^2\left(\frac{\partial \Sigma}{\partial \Delta E^p}\frac{1}{\Delta E^p} - \frac{\Sigma}{(\Delta E^p)^2}\right)\underline{\underline{H}}_{\nabla\varepsilon}\Delta\underline{\nabla\varepsilon}^p\left(\frac{\partial \Delta E^p}{\partial \Delta \underline{\nabla\varepsilon}^p}\right)^T + L_p^2\frac{\Sigma}{\Delta E^p}\underline{\underline{H}}_{\nabla\varepsilon}, \\ \frac{\partial \underline{m}^D}{\partial \Delta \underline{\varepsilon}^p} &= L_p^2\left(\frac{\partial \Sigma}{\partial \Delta E^p}\frac{1}{\Delta E^p} - \frac{\Sigma}{(\Delta E^p)^2}\right)\underline{\underline{H}}_{\nabla\varepsilon}\Delta\underline{\nabla\varepsilon}^p\left(\frac{\partial \Delta E^p}{\partial \Delta \underline{\varepsilon}^p}\right)^T, \end{aligned} \tag{A.9}$$

where

$$\begin{aligned} \frac{\partial \Delta E^p}{\partial \Delta \underline{\varepsilon}^p} &= \frac{2}{3}\frac{1}{\Delta E^p}\underline{\underline{H}}_{\varepsilon}\Delta\underline{\varepsilon}^p, \\ \frac{\partial \Delta E^p}{\partial \Delta \underline{\nabla\varepsilon}^p} &= \frac{L_p^2}{\Delta E^p}\underline{\underline{H}}_{\nabla\varepsilon}\Delta\underline{\nabla\varepsilon}^p. \end{aligned} \tag{A.10}$$

Matrices linking the tensor and Voigt notations are given below

$$\underline{\underline{H_{\nabla\varepsilon}}} = \begin{bmatrix}
1 & 0 & 0 & 0 & 0 & 0 & 0 & 0 & 0 & 0 & 0 & 0 & 0 & 0 & 0 & 0 & 0 & 0 \\
0 & 1 & 0 & 0 & 0 & 0 & 0 & 0 & 0 & 0 & 0 & 0 & 0 & 0 & 0 & 0 & 0 & 0 \\
0 & 0 & 1 & 0 & 0 & 0 & 0 & 0 & 0 & 0 & 0 & 0 & 0 & 0 & 0 & 0 & 0 & 0 \\
0 & 0 & 0 & 1 & 0 & 0 & 0 & 0 & 0 & 0 & 0 & 0 & 0 & 0 & 0 & 0 & 0 & 0 \\
0 & 0 & 0 & 0 & 1 & 0 & 0 & 0 & 0 & 0 & 0 & 0 & 0 & 0 & 0 & 0 & 0 & 0 \\
0 & 0 & 0 & 0 & 0 & 1 & 0 & 0 & 0 & 0 & 0 & 0 & 0 & 0 & 0 & 0 & 0 & 0 \\
0 & 0 & 0 & 0 & 0 & 0 & 1 & 0 & 0 & 0 & 0 & 0 & 0 & 0 & 0 & 0 & 0 & 0 \\
0 & 0 & 0 & 0 & 0 & 0 & 0 & 1 & 0 & 0 & 0 & 0 & 0 & 0 & 0 & 0 & 0 & 0 \\
0 & 0 & 0 & 0 & 0 & 0 & 0 & 0 & 1 & 0 & 0 & 0 & 0 & 0 & 0 & 0 & 0 & 0 \\
0 & 0 & 0 & 0 & 0 & 0 & 0 & 0 & 0 & \frac{1}{2} & 0 & 0 & 0 & 0 & 0 & 0 & 0 & 0 \\
0 & 0 & 0 & 0 & 0 & 0 & 0 & 0 & 0 & 0 & \frac{1}{2} & 0 & 0 & 0 & 0 & 0 & 0 & 0 \\
0 & 0 & 0 & 0 & 0 & 0 & 0 & 0 & 0 & 0 & 0 & \frac{1}{2} & 0 & 0 & 0 & 0 & 0 & 0 \\
0 & 0 & 0 & 0 & 0 & 0 & 0 & 0 & 0 & 0 & 0 & 0 & \frac{1}{2} & 0 & 0 & 0 & 0 & 0 \\
0 & 0 & 0 & 0 & 0 & 0 & 0 & 0 & 0 & 0 & 0 & 0 & 0 & \frac{1}{2} & 0 & 0 & 0 & 0 \\
0 & 0 & 0 & 0 & 0 & 0 & 0 & 0 & 0 & 0 & 0 & 0 & 0 & 0 & \frac{1}{2} & 0 & 0 & 0 \\
0 & 0 & 0 & 0 & 0 & 0 & 0 & 0 & 0 & 0 & 0 & 0 & 0 & 0 & 0 & \frac{1}{2} & 0 & 0 \\
0 & 0 & 0 & 0 & 0 & 0 & 0 & 0 & 0 & 0 & 0 & 0 & 0 & 0 & 0 & 0 & \frac{1}{2} & 0 \\
0 & 0 & 0 & 0 & 0 & 0 & 0 & 0 & 0 & 0 & 0 & 0 & 0 & 0 & 0 & 0 & 0 & \frac{1}{2}
\end{bmatrix},$$

$$\underline{\underline{H_{\varepsilon}}} = \begin{bmatrix}
1 & 0 & 0 & 0 & 0 & 0 \\
0 & 1 & 0 & 0 & 0 & 0 \\
0 & 0 & 1 & 0 & 0 & 0 \\
0 & 0 & 0 & \frac{1}{2} & 0 & 0 \\
0 & 0 & 0 & 0 & \frac{1}{2} & 0 \\
0 & 0 & 0 & 0 & 0 & \frac{1}{2}
\end{bmatrix}. \tag{A.11}$$

## Appendix B. Viscoplastic function

In work [65], the authors have proposed the viscoplastic function (3.26) to be implemented in the following form

$$V(\dot{E}^p) = \begin{cases} \frac{\dot{E}^p}{\varpi \dot{\varepsilon}_0}, & m\dot{E}^p/\dot{E}^p_* \leq 1 \\ \left( \frac{\dot{E}^p - \frac{1-m}{m}\dot{E}^p_*}{\dot{\varepsilon}_0} \right)^m, & m\dot{E}^p/\dot{E}^p_* > 1 \end{cases} \tag{B.1}$$

where threshold effective plastic strain rate is defined by $\dot{E}^p_* = \dot{\varepsilon}_0/(\varpi m)^{1/(m-1)}$. Within numerical analyses in Sections 4 and 5, a small positive regularization parameter $\varpi$ has taken value $\varpi = 0.01$.

## References


[1] R.A. Toupin, Elastic materials with couple-stresses, Arch. Ration. Mech. Anal. 11 (1962) 385–413.
[2] R.D. Mindlin, Micro-structure in linear elasticity, Arch. Ration. Mech. Anal. 16 (1964) 51–78.
[3] R.A. Toupin, Theories of elasticity with couple-stress, Arch. Ration. Mech. Anal. 17 (1964) 85–112.
[4] R. Venkatraman, J.C. Bravman, Separation of film thickness and grain boundary strengthening effects in Al thin films on Si, J. Mater. Res. 7 (8) (1992) 2040–2048.
[5] N. Fleck, G. Muller, M.F. Ashby, J.W. Hutchinson, Strain gradient plasticity: theory and experiment, Acta Metall. Mater. 42 (2) (1994) 475–487.
[6] W.D. Nix, H. Gao, Indentation size effects in crystalline materials: a law for strain gradient plasticity, J. Mech. Phys. Solids 46 (3) (1998) 411–425.
[7] J. Stölken, A. Evans, A microbend test method for measuring the plasticity length scale, Acta Mater. 46 (14) (1998) 5109–5115.
[8] E.C. Aifantis, On the microstructural origin of certain inelastic models, J. Eng. Mater. Technol. 106 (4) (1984) 326–330.
[9] E.C. Aifantis, The physics of plastic deformation, Int. J. Plast. 3 (3) (1987) 211–247.
[10] E.C. Aifantis, On the role of gradients in the localization of deformation and fracture, Internat. J. Engrg. Sci. 30 (1992) 1279–1299.
[11] N. Fleck, J. Hutchinson, A phenomenological theory for strain gradient effects in plasticity, J. Mech. Phys. Solids 41 (12) (1993) 1825–1857.

[12] N. Fleck, J. Hutchinson, Strain gradient plasticity, Adv. Appl. Mech. 33 (1997) 295–361.
[13] N. Fleck, J. Hutchinson, A reformulation of strain gradient plasticity, J. Mech. Phys. Solids 49 (10) (2001) 2245–2271.
[14] P. Gudmundson, A unified treatment of strain gradient plasticity, J. Mech. Phys. Solids 52 (6) (2004) 1379–1406.
[15] M.E. Gurtin, L. Anand, A theory of strain-gradient plasticity for isotropic, plastically irrotational materials. Part I: Small deformations, J. Mech. Phys. Solids 53 (7) (2005) 1624–1649.
[16] M.E. Gurtin, L. Anand, A theory of strain-gradient plasticity for isotropic, plastically irrotational materials. Part II: Finite deformations, Int. J. Plast. 21 (12) (2005) 2297–2318.
[17] M.E. Gurtin, A gradient theory of small-deformation isotropic plasticity that accounts for the Burgers vector and for dissipation due to plastic spin, J. Mech. Phys. Solids 52 (11) (2004) 2545–2568.
[18] M.E. Gurtin, On the plasticity of single crystals: free energy, microforces, plastic-strain gradients, J. Mech. Phys. Solids 48 (5) (2000) 989–1036.
[19] M.E. Gurtin, On a framework for small-deformation viscoplasticity: free energy, microforces, strain gradients, Int. J. Plast. 19 (1) (2003) 47–90.
[20] L. Anand, M. Gurtin, S. Lele, C. Gething, A one-dimensional theory of strain-gradient plasticity: formulation, analysis, numerical results, J. Mech. Phys. Solids 53 (8) (2005) 1789–1826.
[21] M.E. Gurtin, L. Anand, Thermodynamics applied to gradient theories involving the accumulated plastic strain: the theories of Aifantis and Fleck and Hutchinson and their generalization, J. Mech. Phys. Solids 57 (3) (2009) 405–421.
[22] N. Fleck, J. Willis, A mathematical basis for strain-gradient plasticity theory—Part I: Scalar plastic multiplier, J. Mech. Phys. Solids 57 (1) (2009) 161–177.
[23] J.W. Hutchinson, Generalizing J2 flow theory: fundamental issues in strain gradient plasticity, Acta Mech. Sinica 28 (4) (2012) 1078–1086.
[24] H. Gao, Y. Huang, W. Nix, J. Hutchinson, Mechanism-based strain gradient plasticity—I. Theory, J. Mech. Phys. Solids 47 (6) (1999) 1239–1263.
[25] Y. Huang, H. Gao, W. Nix, J. Hutchinson, Mechanism-based strain gradient plasticity—II. Analysis, J. Mech. Phys. Solids 48 (1) (2000) 99–128.
[26] A. Menzel, P. Steinmann, On the continuum formulation of higher gradient plasticity for single and polycrystals, J. Mech. Phys. Solids 48 (8) (2000) 1777–1796.
[27] L. Nicola, Y. Xiang, J.J. Vlassak, E. Van der Giessen, A. Needleman, Plastic deformation of freestanding thin films: experiments and modeling, J. Mech. Phys. Solids 54 (10) (2006) 2089–2110.
[28] D. Liu, Y. He, D.J. Dunstan, B. Zhang, Z. Gan, P. Hu, H. Ding, Toward a further understanding of size effects in the torsion of thin metal wires: An experimental and theoretical assessment, Int. J. Plast. 41 (2013) 30–52.
[29] S. Khakalo, V. Balobanov, J. Niiranen, Modelling size-dependent bending, buckling and vibrations of 2D triangular lattices by strain gradient elasticity models: applications to sandwich beams and auxetics, Internat. J. Engrg. Sci. 127 (2018) 33–52.
[30] S. Khakalo, J. Niiranen, Form II of Mindlin's second strain gradient theory of elasticity with a simplification: For materials and structures from nano- to macro-scales, Eur. J. Mech. A Solids 71 (2018) 292–319.
[31] S. Khakalo, J. Niiranen, Lattice structures as thermoelastic strain gradient metamaterials: Evidence from full-field simulations and applications to functionally step-wise-graded beams, Compos. B. Eng. 177 (2019) 107224.
[32] S. Khakalo, J. Niiranen, Anisotropic strain gradient thermoelasticity for cellular structures: Plate models, homogenization and isogeometric analysis, J. Mech. Phys. Solids 134 (2020) 103728.
[33] H. Yang, D. Timofeev, I. Giorgio, W.H. Müller, Effective strain gradient continuum model of metamaterials and size effects analysis, Contin. Mech. Thermodyn. (2020) http://dx.doi.org/10.1007/S00161-020-00910-3.
[34] T.H. Nguyen, J. Niiranen, A second strain gradient damage model with a numerical implementation for quasi-brittle materials with micro-architectures, Math. Mech. Solids 25 (3) (2020) 515–546.
[35] J. Torabi, J. Niiranen, Microarchitecture-dependent nonlinear bending analysis for cellular plates with prismatic corrugated cores via an anisotropic strain gradient plate theory of first-order shear deformation, Eng. Struct. 236 (2021) 112117.
[36] D. Rayneau-Kirkhope, Stiff auxetics: Hierarchy as a route to stiff, strong lattice based auxetic meta-materials, Sci. Rep. 8 (2018) 12437.
[37] G. Rosi, N. Auffray, Anisotropic and dispersive wave propagation within strain-gradient framework, Wave Motion 63 (2016) 120–134.
[38] G. Rosi, N. Auffray, Continuum modelling of frequency dependent acoustic beam focussing and steering in hexagonal lattices, Eur. J. Mech. A Solids 77 (2019) 103803.
[39] G. Rosi, N. Auffray, C. Combescure, On the failure of classic elasticity in predicting elastic wave propagation in gyroid lattices for very long wavelengths, Symmetry 12 (8) (2020) 1243.
[40] J. Berger, H. Wadley, R. McMeeking, Mechanical metamaterials at the theoretical limit of isotropic elastic stiffness, Nature 543 (2017) 533–537.
[41] T. Tancogne-Dejean, M. Diamantopoulou, M.B. Gorji, C. Bonatti, D. Mohr, 3D Plate-Lattices: An Emerging Class of Low-Density Metamaterial Exhibiting Optimal Isotropic Stiffness, Adv. Mater. 30 (2018) 1803334.
[42] M.-S. Pham, C. Liu, I. Todd, J. Lertthanasarn, Damage-tolerant architected materials inspired by crystal microstructure, Nature 565 (2019) 305–311.
[43] M.C. Fernandes, J. Aizenberg, J.C. Weaver, K. Bertoldi, Mechanically robust lattices inspired by deep-sea glass sponges, Nature Mater. 20 (2021) 237–241.
[44] J.U. Surjadi, L. Gao, H. Du, X. Li, X. Xiong, N.X. Fang, Y. Lu, Mechanical metamaterials and their engineering applications, Adv. Eng. Mater. 21 (2019) 1800864.

[45] R. de Borst, H.-B. Mühlhaus, Gradient-dependent plasticity: Formulation and algorithmic aspects, Internat. J. Numer. Methods Engrg. 35 (1992) 521–539.
[46] R. de Borst, J. Pamin, L. Sluys, Computational issues in gradient plasticity, in: H.-B. Mühlhaus (Ed.), Continuum Models for Materials with Microstructure, Wiley, United States, 1995, pp. 159–200.
[47] Z.C. Xia, J.W. Hutchinson, Crack tip fields in strain gradient plasticity, J. Mech. Phys. Solids 44 (10) (1996) 1621–1648.
[48] J. Shu, N. Fleck, The prediction of a size effect in microindentation, Int. J. Solids Struct. 35 (13) (1998) 1363–1383.
[49] J.Y. Shu, W.E. King, N.A. Fleck, Finite elements for materials with strain gradient effects, Internat. J. Numer. Methods Engrg. 44 (3) (1999) 373–391.
[50] C.F. Niordson, J.W. Hutchinson, Non-uniform plastic deformation of micron scale objects, Internat. J. Numer. Methods Engrg. 56 (7) (2003) 961–975.
[51] P. Fredriksson, P. Gudmundson, L.P. Mikkelsen, Finite element implementation and numerical issues of strain gradient plasticity with application to metal matrix composites, Int. J. Solids Struct. 46 (22–23) (2009) 3977–3987.
[52] K.L. Nielsen, C. Niordson, A 2D finite element implementation of the Fleck–Willis strain-gradient flow theory, Eur. J. Mech. A Solids 41 (2013) 134–142.
[53] N. Fleck, J. Willis, A mathematical basis for strain-gradient plasticity theory. Part II: Tensorial plastic multiplier, J. Mech. Phys. Solids 57 (7) (2009) 1045–1057.
[54] S. Lele, L. Anand, A small-deformation strain-gradient theory for isotropic viscoplastic materials, Phil. Mag. 88 (30–32) (2008) 3655–3689.
[55] C.F. Niordson, B.N. Legarth, Strain gradient effects on cyclic plasticity, J. Mech. Phys. Solids 58 (4) (2010) 542–557.
[56] K. Danas, V.S. Deshpande, N. Fleck, Size effects in the conical indentation of an elasto-plastic solid, J. Mech. Phys. Solids 60 (9) (2012) 1605–1625.
[57] C.F. Dahlberg, J. Faleskog, An improved strain gradient plasticity formulation with energetic interfaces: theory and a fully implicit finite element formulation, Comput. Mech. 51 (5) (2013) 641–659.
[58] L. Bardella, Size effects in phenomenological strain gradient plasticity constitutively involving the plastic spin, Internat. J. Engrg. Sci. 48 (5) (2010) 550–568.
[59] L. Bardella, A. Giacomini, Influence of material parameters and crystallography on the size effects describable by means of strain gradient plasticity, J. Mech. Phys. Solids 56 (9) (2008) 2906–2934.
[60] L. Bardella, A comparison between crystal and isotropic strain gradient plasticity theories with accent on the role of the plastic spin, Eur. J. Mech. A Solids 28 (3) (2009) 638–646.
[61] L. Bardella, A. Panteghini, Modelling the torsion of thin metal wires by distortion gradient plasticity, J. Mech. Phys. Solids 78 (2015) 467–492.
[62] E. Martínez-Pañeda, C.F. Niordson, L. Bardella, A finite element framework for distortion gradient plasticity with applications to bending of thin foils, Int. J. Solids Struct. 96 (2016) 288–299.
[63] A. Panteghini, L. Bardella, On the finite element implementation of higher-order gradient plasticity, with focus on theories based on plastic distortion incompatibility, Comput. Methods Appl. Mech. Engrg. 310 (2016) 840–865.
[64] E. Martínez-Pañeda, V.S. Deshpande, C.F. Niordson, N.A. Fleck, The role of plastic strain gradients in the crack growth resistance of metals, J. Mech. Phys. Solids 126 (2019) 136–150.
[65] S. Fuentes-Alonso, E. Martínez-Pañeda, Fracture in distortion gradient plasticity, Internat. J. Engrg. Sci. 156 (2020) 103369.
[66] S. Forest, Micromorphic approach for gradient elasticity, viscoplasticity, and damage, J. Eng. Mech. 135 (3) (2009) 117–131.
[67] M. Mazière, S. Forest, Strain gradient plasticity modeling and finite element simulation of Lüders band formation and propagation, Contin. Mech. Thermodyn. 27 (1–2) (2015) 83–104.
[68] S. Wulfinghoff, S. Forest, T. Böhlke, Strain gradient plasticity model of the cyclic behavior of laminate microstructures, J. Mech. Phys. Solids 79 (2015) 1–20.
[69] J.-M. Scherer, V. Phalke, J. Besson, S. Forest, J. Hure, B. Tanguy, Lagrange multiplier based vs micromorphic gradient-enhanced rate-(in)dependent crystal plasticity modelling and simulation, Comput. Methods Appl. Mech. Engrg. 372 (2020) 113426.
[70] M. Ryś, S. Forest, H. Petryk, A micromorphic crystal plasticity model with the gradient-enhanced incremental hardening law, Int. J. Plast. 128 (2020) 102655.
[71] G.Z. Voyiadjis, Y. Song, Strain gradient continuum plasticity theories: Theoretical, numerical and experimental investigations, Int. J. Plast. 121 (2019) 21–75.
[72] R. Russo, F.A. Girot Mata, S. Forest, D. Jacquin, A review on strain gradient plasticity approaches in simulation of manufacturing processes, J. Manuf. Mater. Process. 4 (3) (2020) 87.
[73] C. Polizzotto, Strain-gradient elastic-plastic material models and assessment of the higher order boundary conditions, Eur. J. Mech. A Solids 26 (2) (2007) 189–211.
[74] C.F. Niordson, J.W. Hutchinson, On lower order strain gradient plasticity theories, Eur. J. Mech. A Solids 22 (6) (2003) 771–778.
[75] C.F. Niordson, J.W. Kysar, Computational strain gradient crystal plasticity, J. Mech. Phys. Solids 62 (2014) 31–47.
[76] K.L. Nielsen, C.F. Niordson, A numerical basis for strain-gradient plasticity theory: Rate-independent and rate-dependent formulations, J. Mech. Phys. Solids 63 (2014) 113–127.
[77] T.J.R. Hughes, J.A. Cottrell, Y. Bazilevs, Isogeometric analysis: CAD, finite elements, NURBS, exact geometry and mesh refinement, Comput. Methods Appl. Mech. Engrg. 194 (2005) 4135–4195.
[78] H. Gómez, V. Calo, Y. Bazilevs, T.J. Hughes, Isogeometric analysis of the Cahn-Hilliard phase-field model, Comput. Methods Appl. Mech. Engrg. 197 (2008) 4333–4352.
[79] A. Bartezzaghi, L. Dedè, A. Quarteroni, Isogeometric analysis of high order partial differential equations on surfaces, Comput. Methods Appl. Mech. Engrg. 295 (2015) 446–469.

[80] J. Kiendl, K.-U. Bletzinger, J. Linhard, R. Wüchner, Isogeometric shell analysis with Kirchhoff–Love elements, Comput. Methods Appl. Mech. Engrg. 198 (49) (2009) 3902–3914.
[81] C.V. Verhoosel, M.A. Scott, T.J.R. Hughes, R. de Borst, An isogeometric analysis approach to gradient damage models, Internat. J. Numer. Methods Engrg. 86 (2011) 115–134.
[82] M.J. Borden, T.J. Hughes, C.M. Landis, C.V. Verhoosel, A higher-order phase-field model for brittle fracture: Formulation and analysis within the isogeometric analysis framework, Comput. Methods Appl. Mech. Engrg. 273 (2014) 100–118.
[83] L. Beirão da Veiga, T. Hughes, J. Kiendl, C. Lovadina, J. Niiranen, A. Reali, H. Speleers, A locking-free model for Reissner–Mindlin plates: Analysis and isogeometric implementation via NURBS and triangular NURPS, Math. Models Methods Appl. Sci. 25 (2015) 1519–1551.
[84] P. Fischer, M. Klassen, J. Mergheim, P. Steinmann, R. Müller, Isogeometric analysis of 2D gradient elasticity, Comput. Mech. 47 (2011) 325–334.
[85] S. Rudraraju, A.V. der Ven, K. Garikipati, Three-dimensional isogeometric solutions to general boundary value problems of Toupin's gradient elasticity theory at finite strains, Comput. Methods Appl. Mech. Engrg. 278 (2014) 705–728.
[86] J. Niiranen, S. Khakalo, V. Balobanov, A.H. Niemi, Variational formulation and isogeometric analysis for fourth-order boundary value problems of gradient-elastic bar and plane strain/stress problems, Comput. Methods Appl. Mech. Engrg. 308 (2016) 182–211.
[87] I. Kolo, H. Askes, R. de Borst, Convergence analysis of Laplacian-based gradient elasticity in an isogeometric framework, Finite Elem. Anal. Des. 135 (2017) 56–67.
[88] S. Khakalo, J. Niiranen, Isogeometric analysis of higher-order gradient elasticity by user elements of a commercial finite element software, Comput. Aided Des. 82 (2017) 154–169.
[89] R. Makvandi, J.C. Reiher, A. Bertram, D. Juhre, Isogeometric analysis of first and second strain gradient elasticity, Comput. Mech. 61 (3) (2018) 351–363.
[90] J. Niiranen, S. Khakalo, V. Balobanov, Isogeometric finite element analysis of mode I cracks within strain gradient elasticity, J. Struct. Mech. 50 (2017) 337–340.
[91] J. Niiranen, V. Balobanov, J. Kiendl, S. Hosseini, Variational formulations, model comparisons and isogeometric analysis for Euler–Bernoulli micro- and nano-beam models of strain gradient elasticity, Math. Mech. Solids 24 (2019) 312–335.
[92] V. Balobanov, J. Niiranen, Locking-free variational formulations and isogeometric analysis for the Timoshenko beam models of strain gradient and classical elasticity, Comput. Methods Appl. Mech. Engrg. 339 (2018) 137–159.
[93] S. Yaghoubi, V. Balobanov, S. Mousavi, J. Niiranen, Variational formulations and isogeometric analysis for the dynamics of anisotropic gradient-elastic Euler–Bernoulli and shear-deformable beams, Eur. J. Mech. A Solids 69 (2018) 113–123.
[94] L.V. Tran, J. Niiranen, A geometrically nonlinear Euler–Bernoulli beam model within strain gradient elasticity with isogeometric analysis and lattice structure applications, Math. Mech. Complex Syst. 8 (4) (2020) 345–371.
[95] J. Niiranen, J. Kiendl, A.H. Niemi, A. Reali, Isogeometric analysis for sixth-order boundary value problems of gradient-elastic Kirchhoff plates, Comput. Methods Appl. Mech. Engrg. 316 (2017) 328–348.
[96] S. Thai, H.-T. Thai, T.P. Vo, V.I. Patel, Size-dependant behaviour of functionally graded microplates based on the modified strain gradient elasticity theory and isogeometric analysis, Comput. Struct. 190 (2017) 219–241.
[97] V. Balobanov, J. Kiendl, S. Khakalo, J. Niiranen, Kirchhoff–Love shells within strain gradient elasticity: Weak and strong formulations and an $H^3$-conforming isogeometric implementation, Comput. Methods Appl. Mech. Engrg. 344 (2019) 837–857.
[98] I. Kolo, R. de Borst, An isogeometric analysis approach to gradient-dependent plasticity, Internat. J. Numer. Methods Engrg. 113 (2) (2018) 296–310.
[99] I. Kolo, R. de Borst, Dispersion and isogeometric analyses of second-order and fourth-order implicit gradient-enhanced plasticity models, Internat. J. Numer. Methods Engrg. 114 (4) (2018) 431–453.
[100] I. Kolo, L. Chen, R. de Borst, Strain-gradient elasticity and gradient-dependent plasticity with hierarchical refinement of NURBS, Finite Elem. Anal. Des. 163 (2019) 31–43.
[101] R.D. Mindlin, Second gradient of strain and surface-tension in linear elasticity, Int. J. Solids Struct. 1 (1965) 417–438.
[102] C. Polizzotto, A second strain gradient elasticity theory with second velocity gradient inertia – Part I: Constitutive equations and quasi-static behavior, Int. J. Solids Struct. 50 (2013) 3749–3765.
[103] A. Javili, F. dell'Isola, P. Steinmann, Geometrically nonlinear higher-gradient elasticity with energetic boundaries, J. Mech. Phys. Solids 61 (2013) 2381–2401.
[104] G.Z. Voyiadjis, B. Deliktas, Formulation of strain gradient plasticity with interface energy in a consistent thermodynamic framework, Int. J. Plast. 25 (10) (2009) 1997–2024.
[105] M. Lazar, G. Po, The non-singular Green tensor of Mindlin's anisotropic gradient elasticity with separable weak non-locality, Phys. Lett. A 379 (24–25) (2015) 1538–1543.
[106] B.S. Altan, E.C. Aifantis, On some aspects in the special theory of gradient elasticity, J. Mech. Behav. Mater. 8 (1997) 231–282.
[107] C. Polizzotto, A hierarchy of simplified constitutive models within isotropic strain gradient elasticity, Eur. J. Mech. A Solids 61 (2017) 92–109.
[108] E. Bayerschen, T. Böhlke, Power-law defect energy in a single-crystal gradient plasticity framework: a computational study, Comput. Mech. 58 (1) (2016) 13–27.
[109] I. Groma, F. Csikor, M. Zaiser, Spatial correlations and higher-order gradient terms in a continuum description of dislocation dynamics, Acta Mater. 51 (5) (2003) 1271–1281.
[110] S. Forest, N. Guéninchault, Inspection of free energy functions in gradient crystal plasticity, Acta Mech. Sinica 29 (6) (2013) 763–772.
[111] K.J. Bathe, A.P. Cimento, Some practical procedures for the solution of nonlinear finite element equations, Comput. Methods Appl. Mech. Engrg. 22 (1) (1980) 59–85.

[112] J. Bonet, R.D. Wood, Nonlinear Continuum Mechanics for Finite Element Analysis, Cambridge University Press, 1997.
[113] A. Collin, G. Sangalli, T. Takacs, Analysis-suitable G1 multi-patch parametrizations for C1 isogeometric spaces, Comput. Aided Geom. Design 47 (2016) 93–113.
[114] M. Kapl, G. Sangalli, T. Takacs, Construction of analysis-suitable G1 planar multi-patch parameterizations, Comput. Aided Des. 97 (2018) 41–55.
[115] A. Needleman, Material rate dependence and mesh sensitivity in localization problems, Comput. Methods Appl. Mech. Engrg. 67 (1) (1988) 69–85.
[116] G.R. Johnson, W.H. Cook, Fracture characteristics of three metals subjected to various strains, strain rates, temperatures and pressures, Eng. Fract. Mech. 21 (1) (1985) 31–48.
[117] T.J. Hughes, A. Reali, G. Sangalli, Efficient quadrature for NURBS-based isogeometric analysis, Comput. Methods Appl. Mech. Engrg. 199 (5–8) (2010) 301–313.
[118] G. Moutsanidis, W. Li, Y. Bazilevs, Reduced quadrature for FEM, IGA and meshfree methods, Comput. Methods Appl. Mech. Engrg. 373 (2021) 113521.
[119] Dassault Systèmes, Simulia. Abaqus Analysis User's Manual, 20.2.7 Johnson-Cook plasticity, 2009, http://130.149.89.49:2080/v6.9ef/books/usb/default.htm.
[120] G. Po, M. Lazar, N.C. Admal, N. Ghoniem, A non-singular theory of dislocations in anisotropic crystals, Int. J. Plast. 103 (2018) 1–22.
[121] G. Rosi, L. Placidi, N. Auffray, On the validity range of strain-gradient elasticity: a mixed static-dynamic identification procedure, Eur. J. Mech. A Solids 69 (2018) 179–191.
[122] S. Khakalo, J. Niiranen, Gradient-elastic stress analysis near cylindrical holes in a plane under bi-axial tension fields, Int. J. Solids Struct. 110–111 (2017) 351–366.
[123] N. Auffray, H.L. Quang, Q. He, Matrix representations for 3D strain-gradient elasticity, J. Mech. Phys. Solids 61 (2013) 1202–1223.
[124] X. Badiche, S. Forest, T. Guibert, Y. Bienvenu, J.-D. Bartout, P. Ienny, M. Croset, H. Bernet, Mechanical properties and non-homogeneous deformation of open-cell nickel foams: application of the mechanics of cellular solids and of porous materials, Mater. Sci. Eng. A 289 (1–2) (2000) 276–288.
[125] J. Dirrenberger, S. Forest, D. Jeulin, Elastoplasticity of auxetic materials, Comput. Mater. Sci. 64 (2012) 57–61.
[126] F. Fritzen, S. Forest, T. Böhlke, D. Kondo, T. Kanit, Computational homogenization of elasto-plastic porous metals, Int. J. Plast. 29 (2012) 102–119.
[127] L.H. Poh, R. Peerlings, M. Geers, S. Swaddiwudhipong, Towards a homogenized plasticity theory which predicts structural and microstructural size effects, J. Mech. Phys. Solids 61 (11) (2013) 2240–2259.
[128] L. Poh, Scale transition of a higher order plasticity model–A consistent homogenization theory from meso to macro, J. Mech. Phys. Solids 61 (12) (2013) 2692–2710.
[129] L. Poh, V. Phan, Numerical implementation and validation of a consistently homogenized higher order plasticity model, Internat. J. Numer. Methods Engrg. 106 (6) (2016) 454–483.
[130] S. Wulfinghoff, S. Reese, Efficient computational homogenization of simple elastoplastic microstructures using a shear band approach, Comput. Methods Appl. Mech. Engrg. 298 (2016) 350–372.
[131] J. Kochmann, S. Wulfinghoff, L. Ehle, J. Mayer, B. Svendsen, S. Reese, Efficient and accurate two-scale FE-FFT-based prediction of the effective material behavior of elasto-viscoplastic polycrystals, Comput. Mech. 61 (6) (2018) 751–764.
[132] M. Schneider, D. Wicht, T. Böhlke, On polarization-based schemes for the FFT-based computational homogenization of inelastic materials, Comput. Mech. 64 (4) (2019) 1073–1095.
[133] D. Wicht, M. Schneider, T. Böhlke, An efficient solution scheme for small-strain crystal-elasto-viscoplasticity in a dual framework, Comput. Methods Appl. Mech. Engrg. 358 (2020) 112611.
[134] J.-J. Alibert, P. Seppecher, F. Dell'Isola, Truss modular beams with deformation energy depending on higher displacement gradients, Math. Mech. Solids 8 (2003) 51–73.
[135] A. Carcaterra, F. dell'Isola, R. Esposito, M. Pulvirenti, Macroscopic description of microscopically strongly inhomogenous systems: A mathematical basis for the synthesis of higher gradients metamaterials, Arch. Ration. Mech. Anal. 218 (2015) 1239–1262.
[136] F. dell'Isola, I. Giorgio, M. Pawlikowski, Large deformations of planar extensible beams and pantographic lattices: heuristic homogenization, experimental and numerical examples of equilibrium, Proc. R. Soc. A 472 (2016) 20150790.
[137] C. Boutin, F. dell'Isola, I. Giorgio, L. Placidi, Linear pantographic sheets: Asymptotic micro-macro models identification, Math. Mech. Complex Syst. 5 (2) (2017) 127–162.
[138] M. Cuomo, F. Dell'Isola, L. Greco, N. Rizzi, First versus second gradient energies for planar sheets with two families of inextensible fibres: Investigation on deformation boundary layers, discontinuities and geometrical instabilities, Compos. B. Eng. 115 (2017) 423–448.
[139] H. Abdoul-Anziz, P. Seppecher, Strain gradient and generalized continua obtained by homogenizing frame lattices, Math. Mech. Complex Syst. 6 (2018) 213–250.
[140] E. Barchiesi, S. Khakalo, Variational asymptotic homogenization of beam-like square lattice structures, Math. Mech. Solids 24 (10) (2019) 3295–3318.
[141] M. Ambati, J. Kiendl, L. De Lorenzis, Isogeometric Kirchhoff–Love shell formulation for elasto-plasticity, Comput. Methods Appl. Mech. Engrg. 340 (2018) 320–339.
[142] L. Placidi, E. Barchiesi, Energy approach to brittle fracture in strain-gradient modelling, Proc. R. Soc. A 474 (2018) 20170878.
[143] C. Polizzotto, Surface effects, boundary conditions and evolution laws within second strain gradient plasticity, Int. J. Plast. 60 (2014) 197–216.
[144] N.M. Cordero, S. Forest, E.P. Busso, Second strain gradient elasticity of nano-objects, J. Mech. Phys. Solids 97 (2016) 92–124.
[145] A.H. Taheri, K. Suresh, Adaptive w-refinement: A new paradigm in isogeometric analysis, Comput. Methods Appl. Mech. Engrg. 368 (2020) 113180.
[146] E. Martínez-Pañeda, ABAQUS Implementation of strain gradient plasticity, 2019, http://www.empaneda.com/codes/.